POLITECNICO DI TORINO
Repository ISTITUZIONALE

A robust reduced order modeling of mistuned bladed disks: free interface reduction and analytical assembly

Original
A robust reduced order modeling of mistuned bladed disks: free interface reduction and analytical assembly / Usmanov, U., Battiato, G., Firrone, C.M.. - In: COMPUTERS & STRUCTURES. - ISSN 0045-7949. - 332:(2026). [10.1016/j.compstruc.2026.108464]

Availability:
This version is available at: 11583/3016793 since: 2026-10-19T18:08:01Z

Publisher:
Elsevier

Published
DOI:10.1016/j.compstruc.2026.108464

Terms of use:

This article is made available under terms and conditions as specified in the corresponding bibliographic description in the repository

Publisher copyright

(Article begins on next page)

18 November 2026

Computers and Structures 332 (2026) 108464

Contents lists available at ScienceDirect

Computers and Structures

journal homepage: www.elsevier.com/locate/cas

A robust reduced order modeling of mistuned bladed disks: free interface reduction and analytical assembly

Umidjon Usmanov*, Giuseppe Battiato, Christian Maria Firrone

Politecnico di Torino, Corso Duca Degli Abruzzi 24, Turin, 10129, Italy

ARTICLE INFO

Keywords:
Bladed disks
Mistuning
Reduced order models
Free interface reduction
Vibration analysis

ABSTRACT

Bladed disks in turbomachinery are ideally designed as cyclically symmetric structures; however, in practice they are inevitably affected by mistuning arising from manufacturing tolerances, material variability, and service-induced damage. Even small deviations can trigger strong vibration localization and significant amplification of blade responses, making accurate mistuning analysis essential for reliable prediction of dynamic behavior and fatigue life. Although high-fidelity finite element models can capture these effects, their computational cost is often prohibitive, thus motivating the development of reduced-order models (ROMs). Most existing ROMs for mistuned bladed disks are based on fixed-interface formulations, whose retained modal properties depend on boundary conditions and are difficult to identify experimentally. To overcome this limitation, the present work introduces a free-interface-based formulation with explicit analytical assembly. In this work, a novel ROM for mistuned bladed disks is proposed, based on Rubin free-interface reduction method. The proposed framework applies free-interface reduction to the blades, i.e., the only components where mistuning is assumed to be localized. This results in ROMs with a clear physical interpretation, as the reduction basis is formed by free-interface mode shapes that can be identified experimentally without the uncertainties associated with fixture-dependent boundary conditions. An additional contribution is the explicit analytical formulation of both the reduced and assembled matrices, where all matrix partitions are fully expanded and provided in closed form. This yields a comprehensive view of the reduced system and facilitates its evaluation, particularly when computational resources are limited.

1. Introduction

The dynamic response of turbine blades is highly sensitive to small variations in their properties, making the control of mistuning effects a critical challenge in bladed disk design [33]. Mistuning originates from a loss of cyclic symmetry due to blade-to-blade variations in material and geometric properties, which may arise from manufacturing tolerances, material inconsistencies, or in-service degradation. Even minor deviations can produce significant amplification of vibration amplitudes [36,37], increasing the risk of high-cycle fatigue and complicating the prediction of the system response. In particular, certain blades may exhibit strongly localized vibration levels far exceeding those expected in an ideal tuned configuration. This phenomenon is closely related to the fundamental changes that mistuning induces in the modal properties of the system. The breakdown of cyclic symmetry leads to mode splitting and spatial localization of vibration patterns, thereby disrupting the uniform energy distribution typical of tuned structures [16,24]. As a result, the dynamic response becomes dominated by a limited number of blades, whose behavior cannot be reliably inferred from nominal design assumptions. This effect is especially critical under forced excitation, where resonant conditions may arise and persist over narrow frequency ranges [18].

From a modeling standpoint, accurately capturing blade-to-blade variability typically requires high-fidelity finite element (FE) models of the full bladed disk, resulting in large-scale systems with significant computational cost, particularly in the context of probabilistic analyses. Furthermore, the inherently complex relationship between mistuning parameters and the resulting dynamic response adds an additional layer of difficulty to the analysis of mistuned bladed disks.

One of the earliest approaches to the analysis of mistuning in bladed disks is based on lumped-parameter mass–spring models [12–15,18,36]. These simplified representations have been widely used due to their intuitive description of the system dynamics and their ability to capture general trends in the response. Their main advantage lies in their low

* Corresponding author.
Email address: umidjon.usmanov@polito.it (U. Usmanov).

https://doi.org/10.1016/j.compstruc.2026.108464
Received 27 April 2026; Accepted 16 September 2026
Available online 22 September 2026
0045-7949/© 2026 The Author(s). Published by Elsevier Ltd. This is an open access article under the CC BY license (http://creativecommons.org/licenses/by/4.0/).

computational cost, which makes them particularly suitable for large-scale numerical studies, such as Monte Carlo simulations, as well as for gaining qualitative insight into mistuning effects. Moreover, they can be implemented rapidly and require only limited computational resources, making them attractive in the early stages of analysis. Despite these advantages, lumped-parameter models exhibit significant limitations. Their predictions are highly sensitive to small variations in the parameters, which may lead to inaccurate results [15]. Furthermore, they are not able to fully represent the complex structural behavior of real bladed disks, where geometry, boundary conditions, and modal interactions play a crucial role. As the level of detail increases, the number of degrees of freedom (DOFs) required for accuracy grows, making the parameter identification process increasingly challenging and, in many cases, impractical.

An alternative to lumped-parameter formulations is the use of ROMs, which retain a closer representation of the physical structure while significantly reducing the computational cost compared to full finite element analyses. In the literature, two main classes of ROM strategies can be identified for mistuned bladed disks: system-level and component-level approaches [19]. In system-level approaches, the response of the mistuned system is expressed as a linear combination of the modes of the tuned configuration [39]. This strategy captures the essential features of global dynamics and provides a reduction basis that is independent of the specific mistuning pattern. In contrast, component-level approaches perform the reduction at the level of individual components or superelements, such as blades and disk sectors [9]. Mistuning is introduced locally within the component models, and the global system is then assembled from these modified substructures. This approach preserves the physical meaning of the reduction basis and enables a modular representation of the bladed disk. Beyond these two main strategies, an alternative formulation treats mistuning as a structural modification applied to the tuned assembly [26,27]. In this framework, the response of the mistuned system is derived directly from the dynamic characteristics of the tuned configuration—typically expressed in terms of frequency response functions—by introducing a modification matrix that accounts for blade-to-blade variability.

One of the first contributions to the system-level approach was presented by Yang and Griffin [39]. In their work, the mistuned system modes were expressed as linear combinations of a subset of nominal (tuned) system modes, which avoids the need for a FE analysis of the mistuned assembly. The approach laid the foundation for subsequent system-level ROM methods by proving that global mistuning effects could be effectively modeled through a basis derived from tuned system modes. Feiner and Griffin later introduced an important extension of the system-level framework by developing what is now widely referred to as the Fundamental Model of Mistuning (FMM) [17]. Their work simplified the formulation of the Subset of Nominal Modes (SNM) approach by restricting the representation to a single family of modes. This reduction in complexity made the method more practical and easier to apply. FMM requires only minimal input data: the nominal frequencies of the tuned system and the deviations of the individual blade frequencies from their tuned values. This compact formulation allows the mistuning to be fully characterized with two sets of parameters and makes the approach feasible for large-scale studies and Monte Carlo simulations.

Component-level approaches focus on creating the ROMs of the blades and disk separately, with mistuning introduced at the blade level. One of the first contributions in this direction was made by Castanier et al. [9], who proposed a formulation based on component modes of vibration of a single sector. This method leads to compact ROMs that retain the essential disk–blade coupling, allowing mistuning to be introduced directly through the modal stiffness of the blade component. The forced response analysis with the proposed method was carried out by Kruse and Pierre [21]. Their study demonstrated that compact ROMs could efficiently predict mistuned forced vibration amplitudes with good accuracy compared to FE models. Later, Yang and Griffin [38] proposed a ROM that decomposes the bladed disk into substructures, assuming rigid-body motion of blade bases combined with cantilever blade modes. This approach reduced the problem to only six interface DOFs per blade. Bladh et al. extended the reduction method based on component modes to shrouded bladed disks, demonstrating that stiffness mistuning can be introduced efficiently within the reduced-order framework [6]. The same authors then made one of the most influential contributions to the component-based reduced order modeling of mistuned bladed disks. They utilized the Craig–Bampton (CB-CMS) method [10] specifically for cyclically symmetric rotors and introduced two additional techniques: a non-CMS mistuning projection method, which projects mistuning onto tuned system modes, and the novel Secondary Modal Analysis Reduction Technique (SMART), which applies a second reduction step on a CB-CMS model [7]. Later, the same authors validated these methods on small and large FE models, considering both free and forced responses of tuned and mistuned configurations. Their results demonstrated that while the CB-CMS method is robust and reliable, its computational cost is high due to retained boundary DOFs. SMART overcame this limitation, yielding good accuracy with dramatic reductions in model size and computational cost [8]. Lim et al. [22] proposed a generalized component mode mistuning (CMM) framework that represents mistuning as deviations in blade mass and stiffness. The method can handle both small frequency mistuning and large geometric variations, and numerical studies showed that it accurately predicts localization and forced response amplification. Vargiu et al. [34] extended the CMM method by introducing a sector frequency mistuning model. This approach is especially useful when mistuning is not confined to individual blades, such as in blisks or when disk–blade interface effects are significant. More recently, a generalized component-level formulation has been proposed in which blade and disk substructures are reduced separately using an augmented Craig–Bampton framework [20]. This approach enables independent introduction of blade and disk mistuning, including stiffness, damping, and geometric variations, while retaining a modular substructuring strategy based on sector-level FEMs.

Another approach, proposed in [27], formulates mistuning as a structural modification of the tuned bladed disk and establishes an exact relationship between the dynamic responses of the tuned and mistuned systems. Rather than constructing a ROM of the mistuned assembly, the method exploits the frequency response function of the tuned configuration and incorporates mistuning effects through a low-rank modification matrix. This framework allows the mistuned response to be evaluated directly at selected DOFs, without explicit modal truncation or component-level condensation. The tuned system is represented using cyclic symmetry, whereas mistuning is treated as a localized perturbation.

Several works have been dedicated to the development of ROMs for the nonlinear forced response prediction of mistuned bladed disks, particularly focusing on the incorporation of friction contacts. Pourkiaee et al. [30] proposed a ROM for mistuned bladed disks with shroud friction contacts. Their method used Craig–Bampton reduction for blades combined with loaded interface modes for the disk, leading to a compact model built from single-sector calculations. Mashayekhi et al. [25] introduced the Mistuned-Dual (M-Dual) formulation, which merges the component mistuning method with the Dual CMS approach. By employing free-interface and attachment modes, the method avoids assembling full-order matrices and reduces offline costs. Saletti et al. [32] more recently developed a ROM to analyse bladed disks with shroud friction joints under mass mistuning. Their work showed that the proposed formulation can accurately reproduce nonlinear forced responses of mistuned systems with localized contacts. Long and Chen [23] recently developed a Variable-Speed Reduced Order Model (VSROM) for mistuned rotating bladed disks, combining stiffness parameterization with the Component Mode Mistuning method. Assuming weak speed dependence of tuned mode shapes, they proposed a response-based mistuning identification strategy. The method was shown to predict free and forced responses at different speeds.

Despite the many advances in ROM of mistuned bladed disks, the literature has focused primarily on fixed-interface formulations, in which the physical interpretation of retained frequencies depends strongly on boundary conditions and experimental identification is not straightforward. To the best of the authors' knowledge, no works have adopted a free-interface reduction strategy as the foundation for mistuning analysis. The present study fills this gap by introducing a formulation using free component modes, providing explicit analytical forms of the assembled matrices in the reduced-order space, and exploring alternative strategies for mistuning introduction.

In this work, we develop an extended ROM framework for mistuned bladed disks, referred to as the Free-Interface Blade Mistuning (FIBM) method, that builds upon the Rubin free-interface reduction method [31]. The method applies to the components where mistuning is assumed to be localized, i.e., the blades, through the definition of a component-mode matrix which collects a reduced set of free–interface normal modes. Such a reduced modal basis has the advantage of being easily correlated with experimental mode shapes obtained under free conditions, i.e., without considering the uncertainties associated with fixture-dependent boundary conditions. Moreover, unlike most previous studies, the reduced and assembled matrices are not left in compact operator form, but are expanded analytically, showing all partitions explicitly. This provides a clearer view of the reduced system and enables a modular evaluation of the reduced matrices, where individual matrix partitions can be computed independently, thereby reducing the memory requirements of the reduction procedure and facilitating parallel implementation for large-scale finite element models. The proposed framework is validated against an FE model of a mistuned bladed disk, in which mistuning is introduced through blade-to-blade variations of the Young's modulus. Validation is performed by comparing the ROM and FE model in terms of natural frequencies, mode shapes, through the Modal Assurance Criterion (MAC), and forced responses caused by traveling wave Engine-Order (EO) excitation. Although the proposed framework is intended for bladed disks, where friction interfaces are inherently present, the present work focuses on the linear validation of the mistuning formulation. This allows the capability of the proposed method to represent the fundamental effects of mistuning to be assessed independently of nonlinear contact phenomena.

The remainder of the paper is organized as follows. Section 2 presents the proposed ROM framework for mistuned bladed disks. Section 3 is devoted to the validation of the proposed methodology against an FE model, considering both tuned and mistuned configurations, through comparisons of natural frequencies, mode shapes, and EO forced response functions. Finally, Section 4 summarizes the main findings of the study and outlines perspectives for future developments.

2. Methodology

This section presents the FIBM method together with the reduction steps leading to the construction of a ROM of a mistuned bladed disk. The procedure starts from the FE model of the bladed disk in its nominal configuration, which consists of a fundamental disk sector and a blade, representing two physically distinct yet coupled substructures interacting through their shared interfaces. Two different reduction techniques are then employed to derive the ROMs of the disk sector and the blade, respectively: the Craig–Bampton method [10] for the disk sector and the Rubin method [31] for the blade. Finally, the strategy adopted for constructing the full bladed disk ROM, as well as the procedure used to introduce blade mistuning patterns, is presented and discussed.

With reference to the substructures highlighted in green in Fig. 1, the vectors of DOFs for the disk sector and blade can be partitioned as follows:

$$\boldsymbol{x}^S = \begin{Bmatrix} \boldsymbol{x}_e^S \\ \boldsymbol{x}_i^S \\ \boldsymbol{x}_l^S \\ \boldsymbol{x}_h^S \end{Bmatrix}, \quad \boldsymbol{x}^B = \begin{Bmatrix} \boldsymbol{x}_e^B \\ \boldsymbol{x}_i^B \\ \boldsymbol{x}_a^B \end{Bmatrix} \tag{1}$$

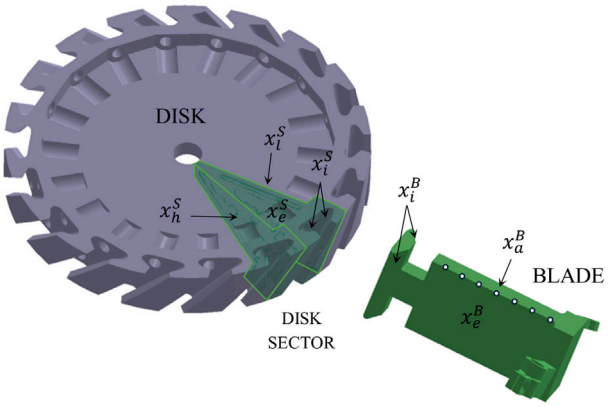


Fig. 1. Schematic representation of the bladed-disk system showing the disk sector and blade component with the definitions of boundary, interface, and auxiliary DOFs.

In this notation, the superscripts S and B designate the DOFs associated with the disk sector and the blade, respectively. The subscript i in both vectors identifies the DOFs located at the blade root joint *interfaces*, i.e., the contact region between the blade and its corresponding slot in the disk (Fig. 1). For the disk sector, the subscripts l and h denote the DOFs of the low and high *frontiers*, respectively. In the case of the blade, the subscript a denotes the *accessory* DOFs, meaning those not directly participating in the interface or structural coupling. The partitions marked with the subscript e in both vectors correspond to the *excess* DOFs, namely those not retained as master DOFs in the reduction. It is also worth noting that each subscript implicitly defines the dimensionality of the corresponding partition; for instance, the subscript i in $\boldsymbol{x}_i^S$ specifies that the vector has size n_i^D. By following the partitioning indicated in Eq. (1), the FE mass and stiffness matrices for the disk sector and blade can be partitioned accordingly as:

$$\boldsymbol{K}^S = \begin{bmatrix} \boldsymbol{K}_{ee}^S & \boldsymbol{K}_{ei}^S & \boldsymbol{K}_{el}^S & \boldsymbol{K}_{eh}^S \\ \boldsymbol{K}_{ie}^S & \boldsymbol{K}_{ii}^S & \boldsymbol{K}_{il}^S & \boldsymbol{K}_{ih}^S \\ \boldsymbol{K}_{le}^S & \boldsymbol{K}_{li}^S & \boldsymbol{K}_{ll}^S & \boldsymbol{K}_{lh}^S \\ \boldsymbol{K}_{he}^S & \boldsymbol{K}_{hi}^S & \boldsymbol{K}_{hl}^S & \boldsymbol{K}_{hh}^S \end{bmatrix}, \quad \boldsymbol{M}^S = \begin{bmatrix} \boldsymbol{M}_{ee}^S & \boldsymbol{M}_{ei}^S & \boldsymbol{M}_{el}^S & \boldsymbol{M}_{eh}^S \\ \boldsymbol{M}_{ie}^S & \boldsymbol{M}_{ii}^S & \boldsymbol{M}_{il}^S & \boldsymbol{M}_{ih}^S \\ \boldsymbol{M}_{le}^S & \boldsymbol{M}_{li}^S & \boldsymbol{M}_{ll}^S & \boldsymbol{M}_{lh}^S \\ \boldsymbol{M}_{he}^S & \boldsymbol{M}_{hi}^S & \boldsymbol{M}_{hl}^S & \boldsymbol{M}_{hh}^S \end{bmatrix} \tag{2}$$

$$\boldsymbol{K}^B = \begin{bmatrix} \boldsymbol{K}_{ee}^B & \boldsymbol{K}_{ei}^B & \boldsymbol{K}_{ea}^B \\ \boldsymbol{K}_{ie}^B & \boldsymbol{K}_{ii}^B & \boldsymbol{K}_{ia}^B \\ \boldsymbol{K}_{ae}^B & \boldsymbol{K}_{ai}^B & \boldsymbol{K}_{aa}^B \end{bmatrix}, \quad \boldsymbol{M}^B = \begin{bmatrix} \boldsymbol{M}_{ee}^B & \boldsymbol{M}_{ei}^B & \boldsymbol{M}_{ea}^B \\ \boldsymbol{M}_{ie}^B & \boldsymbol{M}_{ii}^B & \boldsymbol{M}_{ia}^B \\ \boldsymbol{M}_{ae}^B & \boldsymbol{M}_{ai}^B & \boldsymbol{M}_{aa}^B \end{bmatrix} \tag{3}$$

This structured partitioning provides a clear distinction between the physically meaningful DOFs that must be retained to preserve the system behavior, namely *boundary* DOFs, and those that can be systematically reduced, i.e., *excess* DOFs. For the blade component, the boundary set $\boldsymbol{x}_b^B$ typically includes the DOFs at the blade–root interface and the accessory coordinates, while for the disk sector the boundary set $\boldsymbol{x}_b^S$ includes the blade–root interface DOFs together with the cyclic symmetry frontiers. Excess DOFs will be condensed through the reduction steps presented in the sections below.

$$\boldsymbol{x}_b^S = \begin{Bmatrix} \boldsymbol{x}_i^S \\ \boldsymbol{x}_l^S \\ \boldsymbol{x}_h^S \end{Bmatrix}, \quad \boldsymbol{x}_b^B = \begin{Bmatrix} \boldsymbol{x}_i^B \\ \boldsymbol{x}_a^B \end{Bmatrix} \tag{4}$$

2.1. Blade reduction

The Rubin free-interface reduction method is adopted in this work to reduce the blade component [31]. In this approach, the reduction basis is constructed from two complementary sets of modes. The first

set, referred to as *residual attachment modes* Ψ_r, is obtained as the difference between the full static flexibility of the substructure and the flexibility captured by the retained dynamic modes. For further details on their computation, the reader is referred to [11]. These modes ensure that the static flexibility of the substructure is accurately preserved in the reduced model. The second set consists of the *free-interface normal modes* Φ_f, computed with the boundary degrees of freedom left unconstrained. These modes describe the free–free vibration characteristics of the component and can be directly correlated with experimental modal tests performed under free boundary conditions. In addition, when the component exhibits rigid body motion, a third set of *rigid body modes* Φ_r can be included in the basis to ensure completeness. In the most general case, the displacement vector of the blade can be approximated as:

$$\boldsymbol{x}^B \approx \boldsymbol{\Phi}_r^B \boldsymbol{\eta}_r^B + \boldsymbol{\Phi}_f^B \boldsymbol{\eta}_f^B + \boldsymbol{\Psi}_r^B \boldsymbol{g}_b^B = \begin{bmatrix} \boldsymbol{\Phi}_r^B & \boldsymbol{\Phi}_f^B & \boldsymbol{\Psi}_r^B \end{bmatrix} \begin{Bmatrix} \boldsymbol{\eta}_r^B \\ \boldsymbol{\eta}_f^B \\ \boldsymbol{g}_b^B \end{Bmatrix} = \boldsymbol{R}_R^B \boldsymbol{q}_R^B \tag{5}$$

where $\boldsymbol{R}_R^B$ is the Rubin component-mode matrix, and $\boldsymbol{q}_R^B = \{(\boldsymbol{\eta}_r^B)^T \ (\boldsymbol{\eta}_f^B)^T \ (\boldsymbol{g}_b^B)^T\}^T$ represents the reduced generalized coordinate vector in the Rubin formulation. The vectors $\boldsymbol{\eta}_r^B$ and $\boldsymbol{\eta}_f^B$ are the reduced sets of generalized coordinates associated with the rigid body and free-interface modes, respectively, while $\boldsymbol{g}_b^B$ is the vector of interface forces acting on the boundary DOFs $\boldsymbol{x}_b^B$.

By projecting the blade FE mass and stiffness matrices onto the space spanned by the columns of $\boldsymbol{R}_R^B$, the following ROM is obtained:

$$\begin{aligned} \tilde{\boldsymbol{M}}^B &= \left(\boldsymbol{R}_R^B\right)^T \cdot \boldsymbol{M}^B \cdot \boldsymbol{R}_R^B = \begin{bmatrix} \boldsymbol{I} & \boldsymbol{0} & \boldsymbol{0} \\ \boldsymbol{0} & \boldsymbol{I} & \boldsymbol{0} \\ \boldsymbol{0} & \boldsymbol{0} & \boldsymbol{M}_{r,b}^B \end{bmatrix}, \\ \tilde{\boldsymbol{K}}^B &= \left(\boldsymbol{R}_R^B\right)^T \cdot \boldsymbol{K}^B \cdot \boldsymbol{R}_R^B = \begin{bmatrix} \boldsymbol{0} & \boldsymbol{0} & \boldsymbol{0} \\ \boldsymbol{0} & \boldsymbol{\Omega}_f^2 & \boldsymbol{0} \\ \boldsymbol{0} & \boldsymbol{0} & \boldsymbol{G}_{r,b}^B \end{bmatrix} \end{aligned} \tag{6}$$

where:

$$\boldsymbol{G}_{r,b}^B = \left(\boldsymbol{\Psi}_r^B\right)^T \cdot \boldsymbol{K}^B \cdot \boldsymbol{\Psi}_r^B, \quad \boldsymbol{M}_{r,b}^B = \left(\boldsymbol{\Psi}_r^B\right)^T \cdot \boldsymbol{M}^B \cdot \boldsymbol{\Psi}_r^B \tag{7}$$

are the matrices representing the interface inertia and flexibility associated with the residual flexibility modes at the boundary.

The reduced matrices obtained using the Rubin free-interface method exhibit a clear and physically interpretable structure. As shown in Eq. (6), the reduced stiffness matrix $\tilde{\boldsymbol{K}}^B$ contains a diagonal block corresponding to the squared natural frequencies of the free-interface modes, i.e., $\boldsymbol{\Omega}_f^2$, which is independent of the selection of boundary degrees of freedom. The explicit form of this term is crucial for the formulation of the proposed method, as will be shown in Section 2.6 that mistuning is introduced in the ROM through perturbations of its diagonal entries.

It is worth noting that the Rubin reduction does not directly lead to a standard super-element formulation, since the boundary DOFs are expressed in terms of interface forces $\boldsymbol{g}_b^B$ rather than interface displacements $\boldsymbol{x}_b^B$, as shown in Eq. (5). This formulation, however, can already be employed if one prefers to work in a *dual* form, where the assembly is performed by imposing equilibrium conditions on the boundary forces using Lagrange multipliers [1]. An alternative is the *primal* form of assembly, where compatibility conditions are imposed on the displacements and the equilibrium condition is automatically satisfied by definition. Therefore, a secondary transformation is required to convert the boundary forces into boundary displacements [35]. The authors choose an assembly in a primal form. Such a transformation is found by pre-multiplying Eq. (5) by the Boolean matrix $\boldsymbol{A}$, which selects the component's boundary DOFs $\boldsymbol{x}_b^B$:

$$\boldsymbol{x}_b^B = \boldsymbol{A}\boldsymbol{x}^B = \boldsymbol{A}\left(\boldsymbol{\Phi}_r^B \boldsymbol{\eta}_r^B + \boldsymbol{\Phi}_f^B \boldsymbol{\eta}_f^B + \boldsymbol{\Psi}_r^B \boldsymbol{g}_b^B\right) \tag{8}$$

From this equation, the boundary force DOFs can be expressed as:

$$\boldsymbol{g}_b^B = \boldsymbol{K}_{r,b}^B \left(\boldsymbol{x}_b^B - \boldsymbol{A}\boldsymbol{\Phi}_r^B \boldsymbol{\eta}_r^B - \boldsymbol{A}\boldsymbol{\Phi}_f^B \boldsymbol{\eta}_f^B\right) \tag{9}$$

In this expression, $\boldsymbol{K}_{r,b}^B$ is the residual stiffness corresponding to the boundary DOFs, which can be obtained by applying the matrix $\boldsymbol{A}$ to the residual flexibility matrix, i.e., matrix of residual attachment modes, and taking an inverse:

$$\boldsymbol{K}_{r,b}^B = \left(\boldsymbol{A} \cdot \boldsymbol{\Psi}_r^B\right)^{-1} \tag{10}$$

Therefore, the secondary transformation can be expresed as:

$$\begin{Bmatrix} \boldsymbol{\eta}_r^B \\ \boldsymbol{\eta}_f^B \\ \boldsymbol{g}_b^B \end{Bmatrix} = \begin{bmatrix} \boldsymbol{I} & \boldsymbol{0} & \boldsymbol{0} \\ \boldsymbol{0} & \boldsymbol{I} & \boldsymbol{0} \\ -\boldsymbol{K}_{r,b}^B \boldsymbol{A}\boldsymbol{\Phi}_r^B & -\boldsymbol{K}_{r,b}^B \boldsymbol{A}\boldsymbol{\Phi}_f^B & \boldsymbol{K}_{r,b}^B \end{bmatrix} \begin{Bmatrix} \boldsymbol{\eta}_r^B \\ \boldsymbol{\eta}_f^B \\ \boldsymbol{x}_b^B \end{Bmatrix} = \boldsymbol{T}_2^B \begin{Bmatrix} \boldsymbol{\eta}_r^B \\ \boldsymbol{\eta}_f^B \\ \boldsymbol{x}_b^B \end{Bmatrix} \tag{11}$$

The final reduced mass and stiffness matrices can be obtained from the subsequent application of the reduction steps described from Eqs. (6) to (11):

$$\bar{\boldsymbol{M}}^B = \left(\boldsymbol{T}_2^B\right)^T \cdot \tilde{\boldsymbol{M}}^B \cdot \boldsymbol{T}_2^B, \quad \bar{\boldsymbol{K}}^B = \left(\boldsymbol{T}_2^B\right)^T \cdot \tilde{\boldsymbol{K}}^B \cdot \boldsymbol{T}_2^B \tag{12}$$

$$\bar{\boldsymbol{M}}^B = \begin{bmatrix} \boldsymbol{I} + \left(\boldsymbol{\Phi}_{r|b}^B\right)^T \hat{\boldsymbol{M}}_r^B \boldsymbol{\Phi}_{r|b}^B & \left(\boldsymbol{\Phi}_{r|b}^B\right)^T \hat{\boldsymbol{M}}_r^B \boldsymbol{\Phi}_{f|b}^B & -\left(\boldsymbol{\Phi}_{r|b}^B\right)^T \hat{\boldsymbol{M}}_r^B \\ \left(\boldsymbol{\Phi}_{f|b}^B\right)^T \hat{\boldsymbol{M}}_r^B \boldsymbol{\Phi}_{r|b}^B & \boldsymbol{I} + \left(\boldsymbol{\Phi}_{f|b}^B\right)^T \hat{\boldsymbol{M}}_r^B \boldsymbol{\Phi}_{f|b}^B & -\left(\boldsymbol{\Phi}_{f|b}^B\right)^T \hat{\boldsymbol{M}}_r^B \\ -\hat{\boldsymbol{M}}_r^B \boldsymbol{\Phi}_{r|b}^B & -\hat{\boldsymbol{M}}_r^B \boldsymbol{\Phi}_{f|b}^B & \hat{\boldsymbol{M}}_r^B \end{bmatrix} \tag{13}$$

$$\bar{\boldsymbol{K}}^B = \begin{bmatrix} \left(\boldsymbol{\Phi}_{r|b}^B\right)^T \boldsymbol{K}_{r,b}^B \boldsymbol{\Phi}_{r|b}^B & \left(\boldsymbol{\Phi}_{r|b}^B\right)^T \boldsymbol{K}_{r,b}^B \boldsymbol{\Phi}_{f|b}^B & -\left(\boldsymbol{\Phi}_{r|b}^B\right)^T \boldsymbol{K}_{r,b}^B \\ \left(\boldsymbol{\Phi}_{f|b}^B\right)^T \boldsymbol{K}_{r,b}^B \boldsymbol{\Phi}_{r|b}^B & \boldsymbol{\Omega}_f^2 + \left(\boldsymbol{\Phi}_{f|b}^B\right)^T \boldsymbol{K}_{r,b}^B \boldsymbol{\Phi}_{f|b}^B & -\left(\boldsymbol{\Phi}_{f|b}^B\right)^T \boldsymbol{K}_{r,b}^B \\ -\boldsymbol{K}_{r,b}^B \boldsymbol{\Phi}_{r|b}^B & -\boldsymbol{K}_{r,b}^B \boldsymbol{\Phi}_{f|b}^B & \boldsymbol{K}_{r,b}^B \end{bmatrix} \tag{14}$$

where $\hat{\boldsymbol{M}}_r^B = (\boldsymbol{K}_{r,b}^B)^T \cdot \boldsymbol{M}_{r,b}^B \cdot \boldsymbol{K}_{r,b}^B$ is the condensed residual inertia matrix associated with the residual flexibility modes at the interface. $\boldsymbol{\Phi}_{r|b}^B = \boldsymbol{A} \cdot \boldsymbol{\Phi}_r^B$ and $\boldsymbol{\Phi}_{f|b}^B = \boldsymbol{A} \cdot \boldsymbol{\Phi}_f^B$ denote the partitions of the rigid body and free-interface modes related to the boundary DOFs.

In this representation, the boundary DOFs of the blade comprise two distinct groups: the blade–root interface DOFs $\boldsymbol{x}_i^B$ and the auxiliary DOFs $\boldsymbol{x}_a^B$ (Eq. 4). To ensure compatibility during assembly with the disk, it is convenient to further partition the boundary blocks of the reduced matrices into these corresponding sets. This is achieved by partitioning the mass and stiffness matrices corresponding to boundary DOFs, so that each contribution associated with the blade–root interface and the auxiliary DOFs is treated separately.

$$\begin{aligned} \boldsymbol{K}_{r,b}^B &= \begin{bmatrix} \boldsymbol{K}_{r,b}^{B,ii} & \boldsymbol{K}_{r,b}^{B,ia} \\ \boldsymbol{K}_{r,b}^{B,ai} & \boldsymbol{K}_{r,b}^{B,aa} \end{bmatrix}, \quad \hat{\boldsymbol{M}}_r^B = \begin{bmatrix} \hat{\boldsymbol{M}}_r^{B,ii} & \hat{\boldsymbol{M}}_r^{B,ia} \\ \hat{\boldsymbol{M}}_r^{B,ai} & \hat{\boldsymbol{M}}_r^{B,aa} \end{bmatrix}, \\ \boldsymbol{\Phi}_{f|b}^B &= \begin{Bmatrix} \boldsymbol{\Phi}_{f|b}^{B,i} \\ \boldsymbol{\Phi}_{f|b}^{B,a} \end{Bmatrix}, \quad \boldsymbol{\Phi}_{r|b}^B = \begin{Bmatrix} \boldsymbol{\Phi}_{r|b}^{B,i} \\ \boldsymbol{\Phi}_{r|b}^{B,a} \end{Bmatrix} \end{aligned} \tag{15}$$

So, the reduced mass and stiffness matrices become:

$$\bar{\boldsymbol{M}}^B = \begin{bmatrix} \boldsymbol{I} + \left(\boldsymbol{\Phi}_{r|b}^B\right)^T \hat{\boldsymbol{M}}_r^B \boldsymbol{\Phi}_{r|b}^B & \left(\boldsymbol{\Phi}_{r|b}^B\right)^T \hat{\boldsymbol{M}}_r^B \boldsymbol{\Phi}_{f|b}^B & \left(\boldsymbol{Q}_i^B\right)^T & \left(\boldsymbol{Q}_a^B\right)^T \\ \left(\boldsymbol{\Phi}_{f|b}^B\right)^T \hat{\boldsymbol{M}}_r^B \boldsymbol{\Phi}_{r|b}^B & \boldsymbol{I} + \left(\boldsymbol{\Phi}_{f|b}^B\right)^T \hat{\boldsymbol{M}}_r^B \boldsymbol{\Phi}_{f|b}^B & \left(\boldsymbol{V}_i^B\right)^T & \left(\boldsymbol{V}_a^B\right)^T \\ \boldsymbol{Q}_i^B & \boldsymbol{V}_i^B & \hat{\boldsymbol{M}}_r^{B,ii} & \hat{\boldsymbol{M}}_r^{B,ia} \\ \boldsymbol{Q}_a^B & \boldsymbol{V}_a^B & \hat{\boldsymbol{M}}_r^{B,ai} & \hat{\boldsymbol{M}}_r^{B,aa} \end{bmatrix} \tag{16}$$

$$\bar{\boldsymbol{K}}^B = \begin{bmatrix} \left(\boldsymbol{\Phi}^B_{r|b}\right)^T \boldsymbol{K}^B_{r,b} \boldsymbol{\Phi}^B_{r|b} & \left(\boldsymbol{\Phi}^B_{r|b}\right)^T \boldsymbol{K}^B_{r,b} \boldsymbol{\Phi}^B_{f|b} & \left(\boldsymbol{Z}^B_i\right)^T & \left(\boldsymbol{Z}^B_a\right)^T \\ \left(\boldsymbol{\Phi}^B_{f|b}\right)^T \boldsymbol{K}^B_{r,b} \boldsymbol{\Phi}^B_{r|b} & \boldsymbol{\Omega}^2_f + \left(\boldsymbol{\Phi}^B_{f|b}\right)^T \boldsymbol{K}^B_{r,b} \boldsymbol{\Phi}^B_{f|b} & \left(\boldsymbol{C}^B_i\right)^T & \left(\boldsymbol{C}^B_a\right)^T \\ \boldsymbol{Z}^B_i & \boldsymbol{C}^B_i & \boldsymbol{K}^{B,ii}_{r,b} & \boldsymbol{K}^{B,ia}_{r,b} \\ \boldsymbol{Z}^B_a & \boldsymbol{C}^B_a & \boldsymbol{K}^{B,ai}_{r,b} & \boldsymbol{K}^{B,aa}_{r,b} \end{bmatrix} \tag{17}$$

$$\begin{aligned} \boldsymbol{C}^B_i &= -\boldsymbol{K}^{B,ii}_{r,b} \cdot \boldsymbol{\Phi}^{B,i}_{f|b} - \boldsymbol{K}^{B,ia}_{r,b} \cdot \boldsymbol{\Phi}^{B,a}_{f|b}, & \boldsymbol{Z}^B_i &= -\boldsymbol{K}^{B,ii}_{r,b} \cdot \boldsymbol{\Phi}^{B,i}_{r|b} - \boldsymbol{K}^{B,ia}_{r,b} \cdot \boldsymbol{\Phi}^{B,a}_{r|b} \\ \boldsymbol{C}^B_a &= -\boldsymbol{K}^{B,ai}_{r,b} \cdot \boldsymbol{\Phi}^{B,i}_{f|b} - \boldsymbol{K}^{B,aa}_{r,b} \cdot \boldsymbol{\Phi}^{B,a}_{f|b}, & \boldsymbol{Z}^B_a &= -\boldsymbol{K}^{B,ai}_{r,b} \cdot \boldsymbol{\Phi}^{B,i}_{r|b} - \boldsymbol{K}^{B,aa}_{r,b} \cdot \boldsymbol{\Phi}^{B,a}_{r|b} \\ \boldsymbol{V}^B_i &= -\hat{\boldsymbol{M}}^{B,ii}_r \cdot \boldsymbol{\Phi}^{B,i}_{f|b} - \hat{\boldsymbol{M}}^{B,ia}_r \cdot \boldsymbol{\Phi}^{B,a}_{f|b}, & \boldsymbol{Q}^B_i &= -\hat{\boldsymbol{M}}^{B,ii}_r \cdot \boldsymbol{\Phi}^{B,i}_{r|b} - \hat{\boldsymbol{M}}^{B,ia}_r \cdot \boldsymbol{\Phi}^{B,a}_{r|b} \\ \boldsymbol{V}^B_a &= -\hat{\boldsymbol{M}}^{B,ai}_r \cdot \boldsymbol{\Phi}^{B,i}_{f|b} - \hat{\boldsymbol{M}}^{B,aa}_r \cdot \boldsymbol{\Phi}^{B,a}_{f|b}, & \boldsymbol{Q}^B_a &= -\hat{\boldsymbol{M}}^{B,ai}_r \cdot \boldsymbol{\Phi}^{B,i}_{r|b} - \hat{\boldsymbol{M}}^{B,aa}_r \cdot \boldsymbol{\Phi}^{B,a}_{r|b} \end{aligned} \tag{18}$$

To extend the reduced blade formulation to the full bladed–disk assembly, the reduced matrices of the single blade are systematically replicated across all N sectors. This operation is carried out by means of the Kronecker product between the reduced matrices and the identity matrix of size N, which mathematically distributes the blade dynamics over the entire assembly. The corresponding results can be partitioned accordingly:

$$\begin{aligned} \bar{\boldsymbol{M}}^B_N &= \begin{bmatrix} \boldsymbol{I}_N \otimes \left(\boldsymbol{I} + \left(\boldsymbol{\Phi}^B_{r|b}\right)^T \hat{\boldsymbol{M}}^B_r \boldsymbol{\Phi}^B_{r|b}\right) & \boldsymbol{I}_N \otimes \left(\left(\boldsymbol{\Phi}^B_{r|b}\right)^T \hat{\boldsymbol{M}}^B_r \boldsymbol{\Phi}^B_{f|b}\right) \\ \boldsymbol{I}_N \otimes \left(\boldsymbol{Q}^B_i\right)^T & \boldsymbol{I}_N \otimes \left(\boldsymbol{Q}^B_a\right)^T \\ \boldsymbol{I}_N \otimes \left(\left(\boldsymbol{\Phi}^B_{f|b}\right)^T \hat{\boldsymbol{M}}^B_r \boldsymbol{\Phi}^B_{r|b}\right) & \boldsymbol{I}_N \otimes \left(\boldsymbol{I} + \left(\boldsymbol{\Phi}^B_{f|b}\right)^T \hat{\boldsymbol{M}}^B_r \boldsymbol{\Phi}^B_{f|b}\right) \\ \boldsymbol{I}_N \otimes \left(\boldsymbol{V}^B_i\right)^T & \boldsymbol{I}_N \otimes \left(\boldsymbol{V}^B_a\right)^T \\ \boldsymbol{I}_N \otimes \boldsymbol{Q}^B_i & \boldsymbol{I}_N \otimes \boldsymbol{V}^B_a \\ \boldsymbol{I}_N \otimes \hat{\boldsymbol{M}}^{B,ii}_r & \boldsymbol{I}_N \otimes \hat{\boldsymbol{M}}^{B,ia}_r \\ \boldsymbol{I}_N \otimes \boldsymbol{Q}^B_a & \boldsymbol{I}_N \otimes \boldsymbol{V}^B_a \\ \boldsymbol{I}_N \otimes \hat{\boldsymbol{M}}^{B,ai}_r & \boldsymbol{I}_N \otimes \hat{\boldsymbol{M}}^{B,aa}_r \end{bmatrix} \\ &= \begin{bmatrix} \bar{\boldsymbol{M}}^{B,rr}_N & \bar{\boldsymbol{M}}^{B,rf}_N & \bar{\boldsymbol{M}}^{B,ri}_N & \bar{\boldsymbol{M}}^{B,ra}_N \\ \bar{\boldsymbol{M}}^{B,fr}_N & \bar{\boldsymbol{M}}^{B,ff}_N & \bar{\boldsymbol{M}}^{B,fi}_N & \bar{\boldsymbol{M}}^{B,fa}_N \\ \bar{\boldsymbol{M}}^{B,ir}_N & \bar{\boldsymbol{M}}^{B,if}_N & \bar{\boldsymbol{M}}^{B,ii}_N & \bar{\boldsymbol{M}}^{B,ia}_N \\ \bar{\boldsymbol{M}}^{B,ar}_N & \bar{\boldsymbol{M}}^{B,af}_N & \bar{\boldsymbol{M}}^{B,ai}_N & \bar{\boldsymbol{M}}^{B,aa}_N \end{bmatrix} \end{aligned} \tag{19}$$

$$\begin{aligned} \bar{\boldsymbol{K}}^B_N &= \begin{bmatrix} \boldsymbol{I}_N \otimes \left(\left(\boldsymbol{\Phi}^B_{r|b}\right)^T \cdot \boldsymbol{K}^B_{r,b} \cdot \boldsymbol{\Phi}^B_{r|b}\right) & \boldsymbol{I}_N \otimes \left(\left(\boldsymbol{\Phi}^B_{r|b}\right)^T \cdot \boldsymbol{K}^B_{r,b} \cdot \boldsymbol{\Phi}^B_{f|b}\right) \\ \boldsymbol{I}_N \otimes \left(\boldsymbol{Z}^B_i\right)^T & \boldsymbol{I}_N \otimes \left(\boldsymbol{Z}^B_a\right)^T \\ \boldsymbol{I}_N \otimes \left(\left(\boldsymbol{\Phi}^B_{f|b}\right)^T \cdot \boldsymbol{K}^B_{r,b} \cdot \boldsymbol{\Phi}^B_{r|b}\right) & \boldsymbol{I}_N \otimes \left(\boldsymbol{\Omega}^2_f + \left(\boldsymbol{\Phi}^B_{f|b}\right)^T \cdot \boldsymbol{K}^B_{r,b} \cdot \boldsymbol{\Phi}^B_{f|b}\right) \\ \boldsymbol{I}_N \otimes \left(\boldsymbol{C}^B_i\right)^T & \boldsymbol{I}_N \otimes \left(\boldsymbol{C}^B_a\right)^T \\ \boldsymbol{I}_N \otimes \boldsymbol{Z}^B_i & \boldsymbol{I}_N \otimes \boldsymbol{C}^B_i \\ \boldsymbol{I}_N \otimes \boldsymbol{K}^{B,ii}_{r,b} & \boldsymbol{I}_N \otimes \boldsymbol{K}^{B,ia}_{r,b} \\ \boldsymbol{I}_N \otimes \boldsymbol{Z}^B_a & \boldsymbol{I}_N \otimes \boldsymbol{C}^B_a \\ \boldsymbol{I}_N \otimes \boldsymbol{K}^{B,ai}_{r,b} & \boldsymbol{I}_N \otimes \boldsymbol{K}^{B,aa}_{r,b} \end{bmatrix} \\ &= \begin{bmatrix} \bar{\boldsymbol{K}}^{B,rr}_N & \bar{\boldsymbol{K}}^{B,rf}_N & \bar{\boldsymbol{K}}^{B,ri}_N & \bar{\boldsymbol{K}}^{B,ra}_N \\ \bar{\boldsymbol{K}}^{B,fr}_N & \bar{\boldsymbol{K}}^{B,ff}_N & \bar{\boldsymbol{K}}^{B,fi}_N & \bar{\boldsymbol{K}}^{B,fa}_N \\ \bar{\boldsymbol{K}}^{B,ir}_N & \bar{\boldsymbol{K}}^{B,if}_N & \bar{\boldsymbol{K}}^{B,ii}_N & \bar{\boldsymbol{K}}^{B,ia}_N \\ \bar{\boldsymbol{K}}^{B,ar}_N & \bar{\boldsymbol{K}}^{B,af}_N & \bar{\boldsymbol{K}}^{B,ai}_N & \bar{\boldsymbol{K}}^{B,aa}_N \end{bmatrix} \end{aligned} \tag{20}$$

2.2. Disk sector reduction

The disk sector ROM is obtained by applying the CB-CMS method [10], in which the displacement field of the internal (excess) DOFs is expressed as a linear combination of two complementary sets of component modes. The first set, referred to as *constraint* (or *static*) modes and denoted by $\boldsymbol{\Psi}_{be}$, represents the static deformation patterns obtained by imposing a unit displacement at a boundary DOF while keeping all other boundary DOFs fixed. These modes ensure that the static coupling between the disk and adjacent substructures is accurately preserved. The second set, denoted by $\boldsymbol{\Phi}_{ke}$, consists of a truncated number n_k (with $n_k \ll n_e^D$) of *fixed-interface normal modes* (FINMs), which capture the dynamic flexibility of the substructure under the assumption that the boundary displacement vector $\boldsymbol{x}^S_b$ is fully constrained. By construction, the CB-CMS reduction method relies on partitioning the FE mass and stiffness matrices with respect to boundary and excess DOFs. Considering the DOFs partitioning defined in Eq. (4), the mass and stiffness FE matrices of Eq. (2) can be expressed in a more compact form as:

$$\boldsymbol{K}^S = \begin{bmatrix} \boldsymbol{K}^S_{ee} & \boldsymbol{K}^S_{eb} \\ \boldsymbol{K}^S_{be} & \boldsymbol{K}^S_{bb} \end{bmatrix}, \quad \boldsymbol{M}^S = \begin{bmatrix} \boldsymbol{M}^S_{ee} & \boldsymbol{M}^S_{eb} \\ \boldsymbol{M}^S_{be} & \boldsymbol{M}^S_{bb} \end{bmatrix} \tag{21}$$

The application of the CB-CMS method leads to the following approximation of the physical displacement vector $\boldsymbol{x}^S$:

$$\boldsymbol{x}^S = \begin{Bmatrix} \boldsymbol{x}^S_e \\ \boldsymbol{x}^S_b \end{Bmatrix} = \begin{bmatrix} \boldsymbol{\Phi}^S_{ke} & \boldsymbol{\Psi}^S_{be} \\ \boldsymbol{0}_{bk} & \boldsymbol{I}_{bb} \end{bmatrix} \begin{Bmatrix} \boldsymbol{\eta}^S_k \\ \boldsymbol{x}^S_b \end{Bmatrix} = \boldsymbol{R}^S_{CB}\, \boldsymbol{q}^S_{CB} \tag{22}$$

where $\boldsymbol{R}^S_{CB}$ denotes the CB-CMS component mode matrix, $\boldsymbol{\eta}^S_k$ is the vector of modal amplitudes associated with the reduced set of n_k fixed-interface normal modes, and $\boldsymbol{q}^S_{CB} = \{(\boldsymbol{x}^S_b)^T; (\boldsymbol{\eta}^S_k)^T\}^T$ represents the vector of reduced generalized coordinates in the CB-CMS formulation.

The reduction basis $\boldsymbol{R}^S_{CB}$ is then used to project the full mass and stiffness matrices, $\boldsymbol{M}^S$ and $\boldsymbol{K}^S$, onto the reduced space, yielding the reduced matrices $\tilde{\boldsymbol{M}}^S$ and $\tilde{\boldsymbol{K}}^S$.

$$\begin{aligned} \tilde{\boldsymbol{K}}^S &= \left(\boldsymbol{R}^S_{CB}\right)^T \cdot \boldsymbol{K}^S \cdot \boldsymbol{R}^S_{CB} = \begin{bmatrix} \boldsymbol{\Lambda}^S & \boldsymbol{0} \\ \boldsymbol{0} & \boldsymbol{\kappa}^S_{bb} \end{bmatrix}, \\ \tilde{\boldsymbol{M}}^S &= \left(\boldsymbol{R}^S_{CB}\right)^T \cdot \boldsymbol{M}^S \cdot \boldsymbol{R}^S_{CB} = \begin{bmatrix} \boldsymbol{I}_k & \left(\boldsymbol{\mu}^S_{be}\right)^T \\ \boldsymbol{\mu}^S_{be} & \boldsymbol{\mu}^S_{bb} \end{bmatrix} \end{aligned} \tag{23}$$

where:

$$\begin{aligned} \boldsymbol{\kappa}^S_{bb} &= \boldsymbol{K}^S_{bb} \cdot \boldsymbol{\Psi}^S_{be} + \boldsymbol{K}^S_{be}, \\ \boldsymbol{\mu}^S_{be} &= \left(\boldsymbol{\Psi}^S_{be}\right)^T \cdot \boldsymbol{M}^S_{ee} \cdot \boldsymbol{\Psi}^S_{be} + \boldsymbol{M}^S_{eb} \cdot \boldsymbol{\Psi}^S_{be} + \boldsymbol{M}^S_{be}, \\ \boldsymbol{\mu}^S_{bb} &= \left(\boldsymbol{\Psi}^S_{be}\right)^T \cdot \left(\boldsymbol{M}^S_{ee} \cdot \boldsymbol{\Psi}^S_{be} + \boldsymbol{M}^S_{eb}\right) + \left(\boldsymbol{M}^S_{be}\right)^T \cdot \boldsymbol{\Psi}^S_{be} + \boldsymbol{M}^S_{bb} \end{aligned} \tag{24}$$

To enable an analytical representation of the assembled system, the boundary DOFs of the ROM are partitioned according to their physical roles: the blade–disk interface, the left frontier, and the right frontier. With reference to Eq. (4), the corresponding blocks of the reduced stiffness and mass matrices are partitioned accordingly:

$$\boldsymbol{\kappa}^S_{bb} = \begin{bmatrix} \boldsymbol{\kappa}^S_{ii} & \boldsymbol{\kappa}^S_{il} & \boldsymbol{\kappa}^S_{ih} \\ \boldsymbol{\kappa}^S_{li} & \boldsymbol{\kappa}^S_{ll} & \boldsymbol{\kappa}^S_{lh} \\ \boldsymbol{\kappa}^S_{hi} & \boldsymbol{\kappa}^S_{hl} & \boldsymbol{\kappa}^S_{hh} \end{bmatrix}, \quad \boldsymbol{\mu}^S_{bb} = \begin{bmatrix} \boldsymbol{\mu}^S_{ii} & \boldsymbol{\mu}^S_{il} & \boldsymbol{\mu}^S_{ih} \\ \boldsymbol{\mu}^S_{li} & \boldsymbol{\mu}^S_{ll} & \boldsymbol{\mu}^S_{lh} \\ \boldsymbol{\mu}^S_{hi} & \boldsymbol{\mu}^S_{hl} & \boldsymbol{\mu}^S_{hh} \end{bmatrix}, \quad \boldsymbol{\mu}^S_{be} = \begin{Bmatrix} \boldsymbol{\mu}^S_{ie} \\ \boldsymbol{\mu}^S_{le} \\ \boldsymbol{\mu}^S_{he} \end{Bmatrix} \tag{25}$$

Thus, the reduced mass and stiffness matrices become:

$$\tilde{\boldsymbol{M}}^S = \begin{bmatrix} \boldsymbol{I} & \left(\boldsymbol{\mu}^S_{ie}\right)^T & \left(\boldsymbol{\mu}^S_{le}\right)^T & \left(\boldsymbol{\mu}^S_{he}\right)^T \\ \boldsymbol{\mu}^S_{ie} & \boldsymbol{\mu}^S_{ii} & \boldsymbol{\mu}^S_{il} & \boldsymbol{\mu}^S_{ih} \\ \boldsymbol{\mu}^S_{le} & \boldsymbol{\mu}^S_{li} & \boldsymbol{\mu}^S_{ll} & \boldsymbol{\mu}^S_{lh} \\ \boldsymbol{\mu}^S_{he} & \boldsymbol{\mu}^S_{hi} & \boldsymbol{\mu}^S_{hl} & \boldsymbol{\mu}^S_{hh} \end{bmatrix}, \quad \tilde{\boldsymbol{K}}^S = \begin{bmatrix} \boldsymbol{\Lambda}^S & \boldsymbol{0} & \boldsymbol{0} & \boldsymbol{0} \\ \boldsymbol{0} & \boldsymbol{\kappa}^S_{ii} & \boldsymbol{\kappa}^S_{il} & \boldsymbol{\kappa}^S_{ih} \\ \boldsymbol{0} & \boldsymbol{\kappa}^S_{li} & \boldsymbol{\kappa}^S_{ll} & \boldsymbol{\kappa}^S_{lh} \\ \boldsymbol{0} & \boldsymbol{\kappa}^S_{hi} & \boldsymbol{\kappa}^S_{hl} & \boldsymbol{\kappa}^S_{hh} \end{bmatrix} \tag{26}$$

2.3. Disk sector gram-schmidt frontier reduction

In bladed disk assemblies, the cyclic symmetry frontier DOFs are typically numerous and usually require an additional reduction step. A suitable approach for achieving a more compact representation of the frontier displacements is the Gram–Schmidt Interface (GSI) reduction method [3–5]. According to this method, a selected subset of boundary DOFs can be further processed and approximated using a basis of orthonormal GSI modes. In particular, for the disk sector, the physical displacement partitions $\boldsymbol{x}_l^S$ and $\boldsymbol{x}_h^S$ can be approximated as:

$$\boldsymbol{x}_l^S \approx \boldsymbol{\Theta}_{lw_1}\,\boldsymbol{\eta}_l^S, \quad \boldsymbol{x}_h^S \approx \boldsymbol{\Theta}_{hw_2}\,\boldsymbol{\eta}_h^S \tag{27}$$

where $\boldsymbol{\Theta}_{lw_1}$ and $\boldsymbol{\Theta}_{hw_2}$ denote the truncated sets of GSI modes associated with the low and high disk sector frontiers, respectively. These bases are obtained by applying the Gram–Schmidt orthonormalization procedure to the corresponding partitions (i.e., the low- and high-DOF components) of a reduced set of normal modes, computed by solving the following eigenvalue problem:

$$\left[\boldsymbol{\kappa}_{bb}^S - \omega^2\,\boldsymbol{\mu}_{bb}^S\right]\boldsymbol{\phi} = \boldsymbol{0} \tag{28}$$

Since the FE mesh is identical at both interfaces, compatibility between the GSI modal coordinates of adjacent interfaces (e.g., the high interface of sector $j-1$ and the low interface of sector j) can be enforced during assembly by expressing the displacement fields in a common reduced basis. In practice, the transformation matrix $\boldsymbol{\Theta}_{lw}$ is constructed by first collecting the truncated modal matrices associated with the left and right interfaces, $[\boldsymbol{\Theta}_{lw_1}, \boldsymbol{\Theta}_{hw_2}]$, and then applying a Gram–Schmidt orthonormalization procedure to their columns. This yields a unified set of orthonormal GSI modes, which is used to reduce both interface displacement vectors as:

$$\boldsymbol{x}_l^S \approx \boldsymbol{\Theta}_{lw}\,\boldsymbol{\eta}_l^S, \quad \boldsymbol{x}_h^S \approx \boldsymbol{\Theta}_{lw}\,\boldsymbol{\eta}_h^S \tag{29}$$

Using Eq. (29), the CB-CMS generalized coordinate vector introduced in Eq. (22) can be further reduced as:

$$\begin{Bmatrix}\boldsymbol{\eta}_k^S\\ \boldsymbol{x}_i^S\\ \boldsymbol{x}_l^S\\ \boldsymbol{x}_h^S\end{Bmatrix} = \begin{bmatrix}\boldsymbol{I}_k & \boldsymbol{0} & \boldsymbol{0} & \boldsymbol{0}\\ \boldsymbol{0} & \boldsymbol{I}_i & \boldsymbol{0} & \boldsymbol{0}\\ \boldsymbol{0} & \boldsymbol{0} & \boldsymbol{\Theta}_{lw} & \boldsymbol{0}\\ \boldsymbol{0} & \boldsymbol{0} & \boldsymbol{0} & \boldsymbol{\Theta}_{lw}\end{bmatrix}\begin{Bmatrix}\boldsymbol{\eta}_k^S\\ \boldsymbol{x}_i^S\\ \boldsymbol{\eta}_l^S\\ \boldsymbol{\eta}_h^S\end{Bmatrix} = \boldsymbol{R}_{GSI}^S\,\boldsymbol{q}_{GSI}^S \tag{30}$$

where $\boldsymbol{R}_{GSI}^S$ is the reduction matrix accounting for the GSI reduction of the disk sector frontiers, and $\boldsymbol{q}_{GSI}^S = \{(\boldsymbol{\eta}_k^S)^T\ (\boldsymbol{x}_i^S)^T\ (\boldsymbol{\eta}_l^S)^T\ (\boldsymbol{\eta}_h^S)^T\}^T$ is the reduced generalized coordinate vector in the GSI formulation. The corresponding mass and stiffness matrices after the GSI interface reduction are:

$$\begin{aligned}\boldsymbol{K}_{GSI}^S &= \left(\boldsymbol{R}_{GSI}^S\right)^T\cdot\tilde{\boldsymbol{K}}^S\cdot\boldsymbol{R}_{GSI}^S\\ &= \begin{bmatrix}\boldsymbol{\Lambda}^S & \boldsymbol{0} & \boldsymbol{0} & \boldsymbol{0}\\ \boldsymbol{0} & \boldsymbol{\kappa}_{ii}^S & \boldsymbol{\kappa}_{il}^S\cdot\boldsymbol{\Theta}_{lw} & \boldsymbol{\kappa}_{ih}^S\cdot\boldsymbol{\Theta}_{lw}\\ \boldsymbol{0} & (\boldsymbol{\Theta}_{lw})^T\cdot\boldsymbol{\kappa}_{li}^S & (\boldsymbol{\Theta}_{lw})^T\cdot\boldsymbol{\kappa}_{ll}^S\cdot\boldsymbol{\Theta}_{lw} & (\boldsymbol{\Theta}_{lw})^T\cdot\boldsymbol{\kappa}_{lh}^S\cdot\boldsymbol{\Theta}_{lw}\\ \boldsymbol{0} & (\boldsymbol{\Theta}_{lw})^T\cdot\boldsymbol{\kappa}_{hi}^S & (\boldsymbol{\Theta}_{lw})^T\cdot\boldsymbol{\kappa}_{hl}^S\cdot\boldsymbol{\Theta}_{lw} & (\boldsymbol{\Theta}_{lw})^T\cdot\boldsymbol{\kappa}_{hh}^S\cdot\boldsymbol{\Theta}_{lw}\end{bmatrix}\end{aligned} \tag{31}$$

$$\begin{aligned}\boldsymbol{M}_{GSI}^S &= \left(\boldsymbol{R}_{GSI}^S\right)^T\cdot\tilde{\boldsymbol{M}}^S\cdot\boldsymbol{R}_{GSI}^S\\ &= \begin{bmatrix}\boldsymbol{I} & \left(\boldsymbol{\mu}_{ie}^S\right)^T & \left(\boldsymbol{\mu}_{le}^S\right)^T\cdot\boldsymbol{\Theta}_{lw} & \left(\boldsymbol{\mu}_{he}^S\right)^T\cdot\boldsymbol{\Theta}_{lw}\\ \boldsymbol{\mu}_{ie}^S & \boldsymbol{\mu}_{ii}^S & \boldsymbol{\mu}_{il}^S\cdot\boldsymbol{\Theta}_{lw} & \boldsymbol{\mu}_{ih}^S\cdot\boldsymbol{\Theta}_{lw}\\ (\boldsymbol{\Theta}_{lw})^T\cdot\boldsymbol{\mu}_{le}^S & (\boldsymbol{\Theta}_{lw})^T\cdot\boldsymbol{\mu}_{li}^S & (\boldsymbol{\Theta}_{lw})^T\cdot\boldsymbol{\mu}_{ll}^S\cdot\boldsymbol{\Theta}_{lw} & (\boldsymbol{\Theta}_{lw})^T\cdot\boldsymbol{\mu}_{lh}^S\cdot\boldsymbol{\Theta}_{lw}\\ (\boldsymbol{\Theta}_{lw})^T\cdot\boldsymbol{\mu}_{he}^S & (\boldsymbol{\Theta}_{lw})^T\cdot\boldsymbol{\mu}_{hi}^S & (\boldsymbol{\Theta}_{lw})^T\cdot\boldsymbol{\mu}_{hl}^S\cdot\boldsymbol{\Theta}_{lw} & (\boldsymbol{\Theta}_{lw})^T\cdot\boldsymbol{\mu}_{hh}^S\cdot\boldsymbol{\Theta}_{lw}\end{bmatrix}\end{aligned} \tag{32}$$

2.4. Disk assembly

Once the ROM of a single disk sector has been obtained, the ROM of the full disk can be constructed using one of the following two approaches. The first approach consists of reducing the tuned disk directly in the harmonic space, as described in the Component-Mode-Based ROM for mistuned bladed disks [7]. The second approach, adopted in this work, performs the reduction in the physical space by assembling N sector-level ROMs using Eqs. (31) and (32). For the case considered in this study, both approaches were found to provide comparable accuracy. The physical-space formulation was selected because it provides a clearer physical interpretation of the assembly procedure presented in this work. This also offers greater flexibility for extending the framework to disks with localized geometric modifications or departures from perfect cyclic symmetry, such as holes or other structural features. The assembly is performed by enforcing compatibility of the GSI modal coordinates at the interfaces between adjacent sectors. In this way, displacement continuity across sector interfaces is guaranteed, while equilibrium of interface forces is automatically satisfied by construction [1]. For two adjacent disk sectors, this condition can be expressed as:

$${}^{(j-1)}\boldsymbol{\eta}_h^S = {}^{(j)}\boldsymbol{\eta}_l^S \tag{33}$$

Mathematically, the assembly is carried out through the application of a Boolean connectivity matrix $\boldsymbol{A}^D$, which maps the local boundary DOFs of each sector onto the corresponding global DOFs of the entire structure:

$$\begin{Bmatrix}{}^{(1)}\boldsymbol{\eta}_k^S\\ {}^{(1)}\boldsymbol{x}_i^S\\ {}^{(1)}\boldsymbol{\eta}_l^S\\ {}^{(2)}\boldsymbol{\eta}_h^S\\ {}^{(2)}\boldsymbol{\eta}_k^S\\ {}^{(2)}\boldsymbol{x}_i^S\\ {}^{(2)}\boldsymbol{\eta}_l^S\\ {}^{(2)}\boldsymbol{\eta}_h^S\\ \vdots\\ {}^{(N)}\boldsymbol{\eta}_k^S\\ {}^{(N)}\boldsymbol{x}_i^S\\ {}^{(N)}\boldsymbol{\eta}_l^S\\ {}^{(N)}\boldsymbol{\eta}_h^S\end{Bmatrix} = \boldsymbol{A}^D\begin{Bmatrix}{}^{(1)}\boldsymbol{\eta}_k^S\\ {}^{(2)}\boldsymbol{\eta}_k^S\\ \vdots\\ {}^{(N)}\boldsymbol{\eta}_k^S\\ {}^{(1)}\boldsymbol{\eta}_l^S\\ {}^{(2)}\boldsymbol{\eta}_l^S\\ \vdots\\ {}^{(N)}\boldsymbol{\eta}_l^S\\ {}^{(1)}\boldsymbol{x}_i^S\\ {}^{(2)}\boldsymbol{x}_i^S\\ \vdots\\ {}^{(N)}\boldsymbol{x}_i^S\end{Bmatrix} \tag{34}$$

The full disk assembly matrix $\mathbf{A}^D$ exhibits a distinct regularity that can be captured through a compact algebraic representation based on three Boolean selection matrices, $\mathbf{A}$, $\mathbf{B}$, and $\mathbf{C}$, together with the cyclic permutation operator $\mathbf{P}_N$. The matrices $\mathbf{A}$, $\mathbf{B}$, and $\mathbf{C}$ are Boolean selection matrices that distribute the retained generalized coordinates associated with the blade modal DOFs, the disk frontier DOFs, and the blade–disk interface DOFs, respectively, into the global coordinate vector. Each matrix places the corresponding coordinates of a given sector in their appropriate positions within the assembled system. The cyclic permutation matrix $\mathbf{P}_N$ performs a right cyclic shift of the sector numbering, so that the successive powers of $\mathbf{P}_N$ generate the cyclic repetition of the fundamental sector around the entire bladed disk, leading to the compact assembly operator:

$$\boldsymbol{A}^D = \begin{bmatrix}\boldsymbol{A} & \boldsymbol{B} & \boldsymbol{C}\\ \boldsymbol{A}(\boldsymbol{P}_N\otimes\boldsymbol{I}_f) & \boldsymbol{B}(\boldsymbol{P}_N\otimes\boldsymbol{I}_L) & \boldsymbol{C}(\boldsymbol{P}_N\otimes\boldsymbol{I}_i)\\ \boldsymbol{A}(\boldsymbol{P}_N\otimes\boldsymbol{I}_f)^2 & \boldsymbol{B}(\boldsymbol{P}_N\otimes\boldsymbol{I}_L)^2 & \boldsymbol{C}(\boldsymbol{P}_N\otimes\boldsymbol{I}_i)^2\\ \vdots & \vdots & \vdots\\ \boldsymbol{A}(\boldsymbol{P}_N\otimes\boldsymbol{I}_f)^{N-1} & \boldsymbol{B}(\boldsymbol{P}_N\otimes\boldsymbol{I}_L)^{N-1} & \boldsymbol{C}(\boldsymbol{P}_N\otimes\boldsymbol{I}_i)^{N-1}\end{bmatrix} \tag{35}$$

$$\boldsymbol{A} = \begin{bmatrix}1&0&0&\cdots&0\\0&0&0&\cdots&0\\0&0&0&\cdots&0\\0&0&0&\cdots&0\end{bmatrix},\quad \boldsymbol{B} = \begin{bmatrix}0&0&0&\cdots&0\\0&0&0&\cdots&0\\1&0&0&\cdots&0\\0&1&0&\cdots&0\end{bmatrix},$$

$$\boldsymbol{C} = \begin{bmatrix} 0 & 0 & 0 & \cdots & 0 \\ 1 & 0 & 0 & \cdots & 0 \\ 0 & 0 & 0 & \cdots & 0 \\ 0 & 0 & 0 & \cdots & 0 \end{bmatrix}, \quad \boldsymbol{P}_N = \begin{bmatrix} 0 & 1 & 0 & \cdots & 0 \\ 0 & 0 & 1 & \cdots & 0 \\ \vdots & \vdots & \vdots & \ddots & \vdots \\ 0 & 0 & 0 & \cdots & 1 \\ 1 & 0 & 0 & \cdots & 0 \end{bmatrix} \tag{36}$$

The final reduced mass and stiffness matrices for the full disk become:

$$\boldsymbol{K}^D = (\boldsymbol{A}^D)^T \cdot \left(\boldsymbol{I}_N \otimes \boldsymbol{K}^S_{GSI}\right) \cdot \boldsymbol{A}^D, \quad \boldsymbol{M}^D = (\boldsymbol{A}^D)^T \cdot \left(\boldsymbol{I}_N \otimes \boldsymbol{M}^S_{GSI}\right) \cdot \boldsymbol{A}^D \tag{37}$$

which can be partitioned depending on the set of DOFs they represent, i.e., fixed-interface normal modes ($\boldsymbol{\eta}^D_k = \{ {}^{(1)}\boldsymbol{\eta}^S_k \ {}^{(2)}\boldsymbol{\eta}^S_k \ \dots \ {}^{(N)}\boldsymbol{\eta}^S_k \}$), truncated set of GSI modes ($(\boldsymbol{\eta}^D_l = \{ {}^{(1)}\boldsymbol{\eta}^S_l \ {}^{(2)}\boldsymbol{\eta}^S_l \ \dots \ {}^{(N)}\boldsymbol{\eta}^S_l \})$) at the interface and physical displacements at the blade root ($(\boldsymbol{x}^D_i = \{ {}^{(1)}\boldsymbol{x}^S_i \ {}^{(2)}\boldsymbol{x}^S_i \ \dots \ {}^{(N)}\boldsymbol{x}^S_i \})$), as follows:

$$\boldsymbol{K}^D = \begin{bmatrix} \boldsymbol{K}^D_{kk} & \boldsymbol{K}^D_{kL} & \boldsymbol{K}^D_{ki} \\ (\boldsymbol{K}^D_{kL})^T & \boldsymbol{K}^D_{LL} & \boldsymbol{K}^D_{Li} \\ (\boldsymbol{K}^D_{ki})^T & (\boldsymbol{K}^D_{Li})^T & \boldsymbol{K}^D_{ii} \end{bmatrix}, \quad \boldsymbol{M}^D = \begin{bmatrix} \boldsymbol{M}^D_{kk} & \boldsymbol{M}^D_{kL} & \boldsymbol{M}^D_{ki} \\ (\boldsymbol{M}^D_{kL})^T & \boldsymbol{M}^D_{LL} & \boldsymbol{M}^D_{Li} \\ (\boldsymbol{M}^D_{ki})^T & (\boldsymbol{M}^D_{Li})^T & \boldsymbol{M}^D_{ii} \end{bmatrix} \tag{38}$$

With reference to the reduced stiffness matrix $\boldsymbol{K}^D$, its partitions can be explicitely expressed as:

$$\begin{aligned}
\boldsymbol{K}^D_{kk} &= \sum_{j=0}^{N-1} (\boldsymbol{P}_N \otimes \boldsymbol{I}_f)^{jT} \boldsymbol{A}^T \boldsymbol{K}^S_{GSI} \boldsymbol{A} (\boldsymbol{P}_N \otimes \boldsymbol{I}_f)^j, \\
\boldsymbol{K}^D_{kL} &= \sum_{j=0}^{N-1} (\boldsymbol{P}_N \otimes \boldsymbol{I}_f)^{jT} \boldsymbol{A}^T \boldsymbol{K}^S_{GSI} \boldsymbol{B} (\boldsymbol{P}_N \otimes \boldsymbol{I}_L)^j, \\
\boldsymbol{K}^D_{LL} &= \sum_{j=0}^{N-1} (\boldsymbol{P}_N \otimes \boldsymbol{I}_L)^{jT} \boldsymbol{B}^T \boldsymbol{K}^S_{GSI} \boldsymbol{B} (\boldsymbol{P}_N \otimes \boldsymbol{I}_L)^j, \\
\boldsymbol{K}^D_{ki} &= \sum_{j=0}^{N-1} (\boldsymbol{P}_N \otimes \boldsymbol{I}_f)^{jT} \boldsymbol{A}^T \boldsymbol{K}^S_{GSI} \boldsymbol{C} (\boldsymbol{P}_N \otimes \boldsymbol{I}_i)^j, \\
\boldsymbol{K}^D_{Li} &= \sum_{j=0}^{N-1} (\boldsymbol{P}_N \otimes \boldsymbol{I}_L)^{jT} \boldsymbol{B}^T \boldsymbol{K}^S_{GSI} \boldsymbol{C} (\boldsymbol{P}_N \otimes \boldsymbol{I}_i)^j, \\
\boldsymbol{K}^D_{ii} &= \sum_{j=0}^{N-1} (\boldsymbol{P}_N \otimes \boldsymbol{I}_i)^{jT} \boldsymbol{C}^T \boldsymbol{K}^S_{GSI} \boldsymbol{C} (\boldsymbol{P}_N \otimes \boldsymbol{I}_i)^j.
\end{aligned} \tag{39}$$

The mass matrix partitions are obtained in an analogous manner by replacing $\boldsymbol{K}^S_{GSI}$ with $\boldsymbol{M}^S_{GSI}$ in Eq. (39).

2.5. Bladed disk assembly

The full bladed-disk ROM is obtained by imposing compatibility between the blade–root DOFs, i.e., $\boldsymbol{x}^D_i$ and $\boldsymbol{x}^B_{N,i}$, belonging between disk ROM and the reduced blade components:

$$\begin{Bmatrix} \boldsymbol{\eta}^D_k \\ \boldsymbol{\eta}^D_L \\ \boldsymbol{x}^D_i \\ \boldsymbol{\eta}^B_{N,r} \\ \boldsymbol{\eta}^B_{N,f} \\ \boldsymbol{x}^B_{N,i} \\ \boldsymbol{x}^B_{N,a} \end{Bmatrix} = \begin{bmatrix} \mathbf{1} & \mathbf{0} & \mathbf{0} & \mathbf{0} & \mathbf{0} & \mathbf{0} \\ \mathbf{0} & \mathbf{1} & \mathbf{0} & \mathbf{0} & \mathbf{0} & \mathbf{0} \\ \mathbf{0} & \mathbf{0} & \mathbf{1} & \mathbf{0} & \mathbf{0} & \mathbf{0} \\ \mathbf{0} & \mathbf{0} & \mathbf{0} & \mathbf{1} & \mathbf{0} & \mathbf{0} \\ \mathbf{0} & \mathbf{0} & \mathbf{0} & \mathbf{0} & \mathbf{1} & \mathbf{0} \\ \mathbf{0} & \mathbf{0} & \mathbf{1} & \mathbf{0} & \mathbf{0} & \mathbf{0} \\ \mathbf{0} & \mathbf{0} & \mathbf{0} & \mathbf{0} & \mathbf{0} & \mathbf{1} \end{bmatrix} \begin{Bmatrix} \boldsymbol{\eta}^D_k \\ \boldsymbol{\eta}^D_L \\ \boldsymbol{x}_i \\ \boldsymbol{\eta}^B_{N,r} \\ \boldsymbol{\eta}^B_{N,f} \\ \boldsymbol{x}^B_{N,a} \end{Bmatrix} = \boldsymbol{A}_{bd}\, \boldsymbol{q}_{bd} \tag{40}$$

where $\boldsymbol{A}_{bd}$ is the global assembly matrix, and $\boldsymbol{q}_{bd} = \{(\boldsymbol{\eta}^D_k)^T \ (\boldsymbol{\eta}^D_L)^T \ (\boldsymbol{x}_i)^T \ (\boldsymbol{\eta}^B_{N,r})^T \ (\boldsymbol{\eta}^B_{N,f})^T \ (\boldsymbol{x}^B_{N,a})^T\}^T$ thus represents the reduced generalized coordinate vector of the full assembly.

The corresponding mass and stiffness matrices for the assembled bladed disk are

$$\boldsymbol{K}_{bd} = (\boldsymbol{A}_{bd})^T \begin{bmatrix} \boldsymbol{K}^D & \mathbf{0} \\ \mathbf{0} & \bar{\boldsymbol{K}}^B_N \end{bmatrix} \boldsymbol{A}_{bd}, \quad \boldsymbol{M}_{bd} = (\boldsymbol{A}_{bd})^T \begin{bmatrix} \boldsymbol{M}^D & \mathbf{0} \\ \mathbf{0} & \bar{\boldsymbol{M}}^B_N \end{bmatrix} \boldsymbol{A}_{bd} \tag{41}$$

Accordingly, the constituents of the assembled blade–disk stiffness matrix can be written explicitly in block-partitioned form as follows:

$$\boldsymbol{K}_{\mathrm{bd}} = \begin{bmatrix} \boldsymbol{K}^D_{kk} & \boldsymbol{K}^D_{kL} & \boldsymbol{K}^D_{ki} & \mathbf{0} & \mathbf{0} & \mathbf{0} \\ (\boldsymbol{K}^D_{kL})^T & \boldsymbol{K}^D_{LL} & \boldsymbol{K}^D_{Li} & \mathbf{0} & \mathbf{0} & \mathbf{0} \\ (\boldsymbol{K}^D_{ki})^T & (\boldsymbol{K}^D_{Li})^T & \boldsymbol{K}^D_{ii} + \bar{\boldsymbol{K}}^{B,ii}_N & \bar{\boldsymbol{K}}^{B,ir}_N & \bar{\boldsymbol{K}}^{B,if}_N & \bar{\boldsymbol{K}}^{B,ia}_N \\ \mathbf{0} & \mathbf{0} & \bar{\boldsymbol{K}}^{B,ri}_N & \bar{\boldsymbol{K}}^{B,rr}_N & \bar{\boldsymbol{K}}^{B,rf}_N & \bar{\boldsymbol{K}}^{B,ra}_N \\ \mathbf{0} & \mathbf{0} & \bar{\boldsymbol{K}}^{B,fi}_N & \bar{\boldsymbol{K}}^{B,fr}_N & \bar{\boldsymbol{K}}^{B,ff}_N & \bar{\boldsymbol{K}}^{B,fa}_N \\ \mathbf{0} & \mathbf{0} & \bar{\boldsymbol{K}}^{B,ai}_N & \bar{\boldsymbol{K}}^{B,ar}_N & \bar{\boldsymbol{K}}^{B,af}_N & \bar{\boldsymbol{K}}^{B,aa}_N \end{bmatrix} \tag{42}$$

The corresponding mass matrix constituents are obtained in an analogous manner by replacing the stiffness submatrices with their mass counterparts.

At this stage, once the full bladed disk assembly has been obtained in physical coordinates, the user has the possibility of applying an additional reduction of the blade-root interface DOFs [2]. This step is optional and depends on the number of interface DOFs retained at the blade root. If the number of these DOFs is already sufficiently small, the model can be considered complete, and no further reduction is required. However, if the interface DOFs remain relatively large, applying this additional reduction provides a more compact representation.

2.6. Mistuning modeling

Mistuning is introduced by perturbing the eigenvalues corresponding to the free vibration modes of each blade, i.e., the diagonal entries in the bidiagonal block matrix $\boldsymbol{\Omega}^2_f$, in Eq. (20). Specifically, the ROM is constructed by modifying the retained free-interface modal frequencies, while assuming that the corresponding mode shapes remain unchanged. This assumption implies that mistuning primarily affects the modal stiffness, with negligible influence on the mode shapes. As a result, each blade is assigned a distinct dynamic signature without altering the reduction basis or the assembly procedure. Consequently, the mass and stiffness matrices of the full bladed disk retain a closed analytical form, since only a well-defined partition of the stiffness matrix is affected by the perturbation. This formulation provides a straightforward and efficient means of controlling blade-to-blade variability and is strongly compatible with experimental data, as free-interface natural frequencies can be readily identified through experimental modal testing and directly incorporated into the ROM.

In the assembled stiffness matrix (see Eq. 42), the eigenvalues of the blade free-interface normal modes appear explicitly in the partition $\bar{\boldsymbol{K}}^{B,ff}_N$:

$$\bar{\boldsymbol{K}}^{B,ff}_N = \boldsymbol{I}_N \otimes \left(\boldsymbol{\Omega}^B_f\right)^2 + \boldsymbol{I}_N \otimes \left(\left(\boldsymbol{\Phi}^B_{f|b}\right)^T \cdot \boldsymbol{K}^B_{r,b} \cdot \boldsymbol{\Phi}^B_{f|b}\right) \tag{43}$$

where $\boldsymbol{I}_N \otimes (\boldsymbol{\Omega}^B_f)^2$ is block diagonal across the blades, with $(\boldsymbol{\Omega}^B_f)^2 = \mathrm{diag}(\omega^2_{f,1}, \omega^2_{f,2}, \dots, \omega^2_{f,n_f})$, and n_f denotes the number of retained free-interface modes per blade. Each blade ROM $j = 1, 2, \dots, N$ is thus associated with a diagonal sub-block of size $n_f \times n_f$, which is identical in the tuned configuration. Mistuning is incorporated into the ROM by perturbing the entries of these sub-blocks via the parameters ξ_j. For

the j-th blade, the frequency perturbation is defined as:

$$\left(\hat{\boldsymbol{\Omega}}^{B}_{f,j}\right)^2 = \mathrm{diag}\left[(1+\xi_{j,1})\,\omega^2_{f,1},\,(1+\xi_{j,2})\,\omega^2_{f,2},\,\ldots,\,(1+\xi_{j,n_f})\,\omega^2_{f,n_f}\right], \quad (44)$$

Assembling over all blades leads to:

$$\boldsymbol{I}_N \otimes \left(\hat{\boldsymbol{\Omega}}^{B}_{f}\right)^2 = \bigoplus_{i=1}^{N}\left(\hat{\boldsymbol{\Omega}}^{B}_{f,i}\right)^2 = \mathrm{diag}\left[\left(\hat{\boldsymbol{\Omega}}^{B}_{f,1}\right)^2,\left(\hat{\boldsymbol{\Omega}}^{B}_{f,2}\right)^2,\ldots,\left(\hat{\boldsymbol{\Omega}}^{B}_{f,N}\right)^2\right] \quad (45)$$

This formulation is highly flexible since each blade can be assigned its own mistuning pattern, and each retained mode on a given blade can be perturbed independently. It also aligns naturally with experimental practice, since the required free-free natural frequencies can be identified from standard modal tests and mapped directly into the diagonal entries.

3. Results and discussions

This section evaluates the accuracy and computational efficiency of the proposed FIBM ROM framework through two representative test cases: (i) a nominally tuned bladed disk, for which the solution can be efficiently obtained by exploiting cyclic symmetry, and (ii) a mistuned bladed disk, where blade-to-blade variability breaks cyclic symmetry and requires full system assembly.

The reference FE model used for validation is shown in Fig. 2. The fundamental sector, depicted in Fig. 2(a), consists of one disk sector and one nominal blade, and serves as the basis for both the reduction and cyclic assembly procedures. The corresponding full bladed-disk model, obtained by periodic repetition of the fundamental sector, is shown in Fig. 2(b). This model represents a numerical counterpart to the academic bladed disk investigated experimentally in [28,29], and is adopted here as the reference solution.

For the tuned configuration, the size of the full FE model and the dimensionality reduction achieved by the proposed approach are first discussed. The accuracy of the ROM is then assessed by comparing its natural frequencies with those of the full FE model.

The analysis is subsequently extended to the mistuned case. Blade mistuning is introduced in the full FE model, and the corresponding mistuned ROM is constructed using the proposed methodology. Validation is carried out through a comparison of natural frequencies, mode shapes (via MAC values), and EO forced response functions, demonstrating the capability of the proposed approach to accurately capture the dynamic behavior of mistuned bladed disks.

3.1. Tuned bladed disk

Prior to reduction, the disk sector FEM contains 47,217 DOFs, while the blade component FEM consists of 160,245 DOFs. The assembly of all sectors leads to a full bladed-disk FE model with a total of 1,217,856 DOFs. The resulting system size makes full-order dynamic analyses computationally demanding and therefore provides a suitable benchmark for assessing both the accuracy and the efficiency of the reduced-order model. The DOF distribution of the disk sector, blade component, and full assembly is summarized in Table 1.

The reduction procedures applied to the disk sector and blade component follow the formulations introduced in Section 2. The disk sector is reduced using the CB-CMS method, while the blade component is reduced independently using the Rubin free-interface method. The accuracy of these reductions is assessed by comparing the natural frequencies of the reduced-order models with those of the corresponding full FE models, as shown in Fig. 3(a) for the disk sector and Fig. 3(b) for the blade component.

For the CB–CMS reduction, the accuracy is higher for lower-frequency modes and gradually deteriorates for higher modes [10]. The number of retained fixed-interface modes was determined through a sensitivity analysis, which identified 50 modes per sector as the best compromise between accuracy and model size over the frequency range of interest. As shown in Fig. 3(a), this choice results in a maximum relative error below approximately 1%. In contrast, for the Rubin free-interface reduction, increasing the number of retained modes did not provide a noticeable improvement in accuracy. A sensitivity analysis indicated that retaining 20 modes is sufficient to capture the relevant dynamics. As illustrated in Fig. 3(b), the corresponding error remains below approximately 0.03%.

Following the component-level reduction, the disk sector frontier DOFs are further reduced using the GSI method described in Section 2.3. A sensitivity analysis on the number of retained GSI modes is performed on the full disk assembly and is reported in Fig. 4(a), where the natural frequencies of the reduced model are compared with those of the full FE model over the first 100 modes. As shown, the accuracy improves with the number of retained GSI modes but reaches a saturation point beyond approximately 50 modes, after which no significant improvement is observed. This trend is further confirmed by the mean error reported in Fig. 4(b), where a value of approximately 0.52% is obtained for 50 GSI modes. Since this level of accuracy is considered sufficient and further increases in the number of modes would increase the system size without significant improvement in accuracy, 50 GSI modes are retained.

The accuracy of the proposed ROM is then assessed by comparing the natural frequencies of the tuned ROM, with those obtained from the FE modal analysis (Fig. 2b). In particular, the first 100 natural frequencies are considered, and the relative error is evaluated in terms of percentage difference with respect to the full-order reference solution. As shown in Fig. 5, the mode-wise error on the natural frequencies remains below 0.1% for the vast majority of the modes, indicating an excellent agreement between the reduced and full-order models. A limited number of localized peaks is observed, with maximum error values

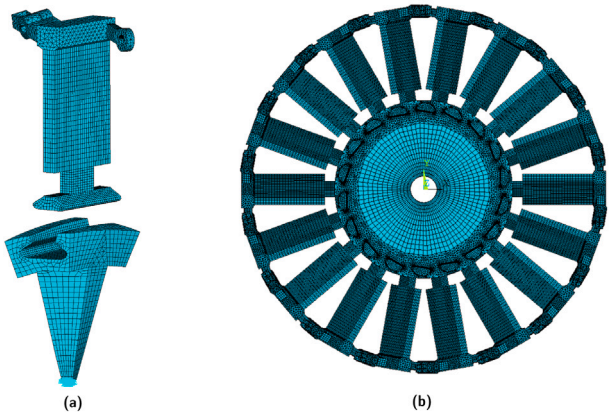


Fig. 2. FE reference model: (a) fundamental sector (disk sector and blade); (b) full bladed-disk FE model.

Table 1
Degrees of freedom (DOFs) of the FE model prior to reduction.

Component	DOFs
Disk sector – internal	41,841
Disk sector – blade–root interface	744
Disk sector – left frontier	2316
Disk sector – right frontier	2316
Disk sector – total	**47,217**
Blade – internal	159,441
Blade – blade–root interface	744
Blade – accessory	60
Blade – total	**160,245**
Full bladed disk (assembled)	**1,217,856**

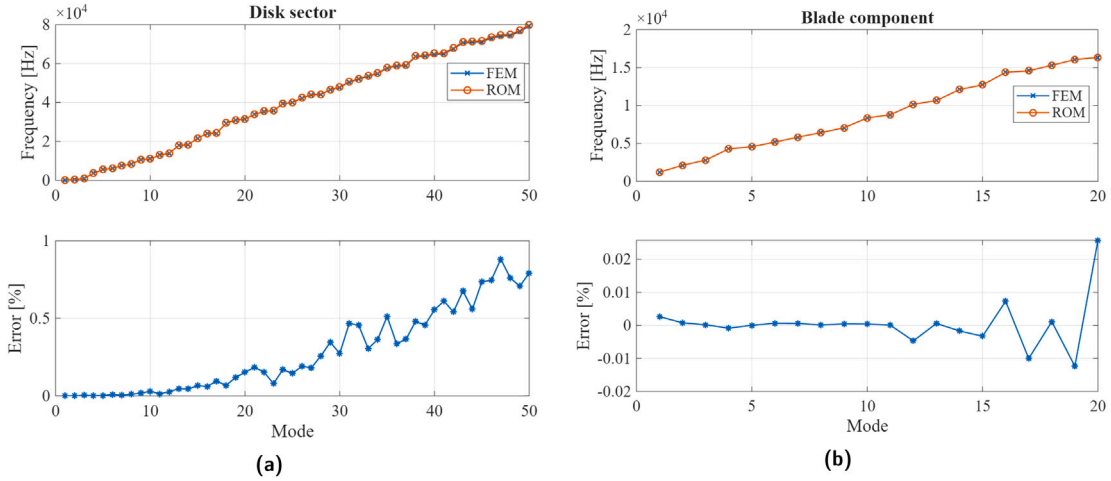


Fig. 3. Comparison of natural frequencies between the ROM and the full FE model: (a) disk sector (CB–CMS reduction) and (b) blade component (Rubin reduction).

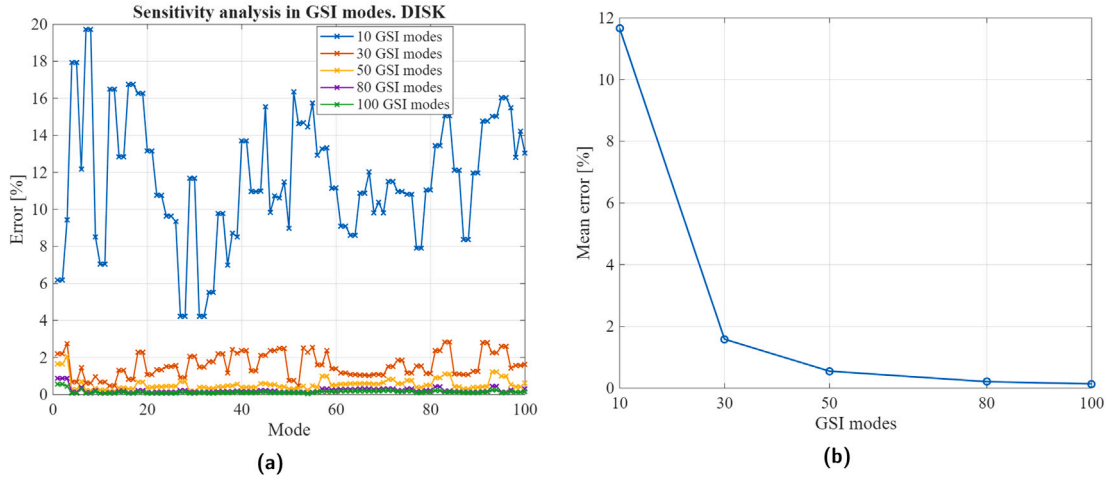


Fig. 4. Sensitivity analysis of GSI reduction: (a) frequency error for different numbers of retained GSI modes and (b) corresponding mean error over the first 100 modes.

remaining below 1%. The mean error level, also reported in the figure, stays well below 0.1%, confirming that the ROM accurately reproduces the global dynamic behavior of the system.

3.2. Mistuned case

In this subsection, the performance of the FIBM ROM is assessed in the presence of mistuning. The reference model is an FE model in which mistuning is introduced at the blade level through variations in Young modulus with respect to its nominal value, while the disk is kept nominally tuned. The Young modulus of each blade is assumed to be a random variable sampled from a normal distribution with a mean value equal to the nominal material property. Two levels of standard deviation are considered, namely 3% and 10% of the nominal value, which are representative of small and large mistuning levels that may naturally occur in bladed disks due to manufacturing tolerances or material inhomogeneities [32]. To avoid introducing a global stiffness shift, the sample mean of the generated mistuning pattern is enforced to coincide with the mean of the underlying distribution. The resulting blade-to-blade variations of the Young modulus for the considered mistuning realizations are illustrated in Fig. 6.

The introduction of mistuning in the ROM starts from the reduced mass and stiffness matrices of the nominally tuned assembly. In the present approach, mistuning is introduced as a perturbation of the free-interface natural frequencies of the blade component, following the

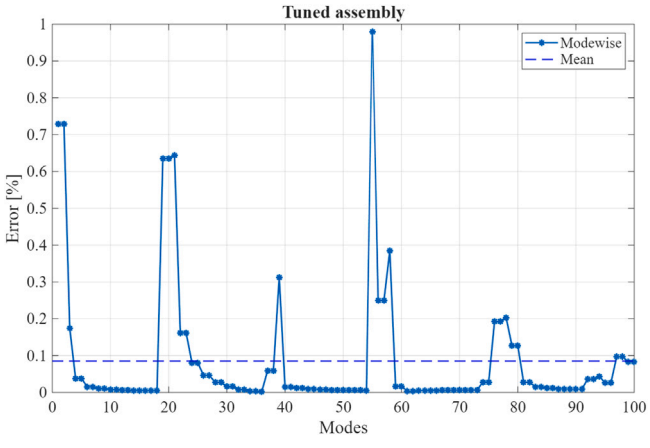


Fig. 5. Mode-wise percentage absolute error between the tuned natural frequencies predicted by the ROM and the full FE model for the first 100 modes.

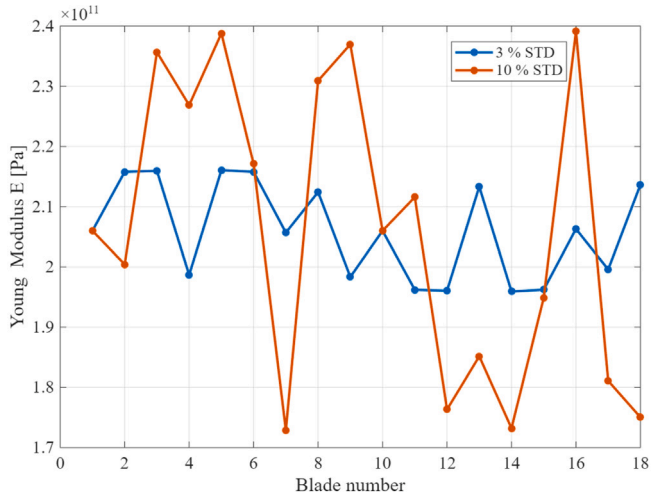


Fig. 6. Blade-to-blade variation of Young's modulus used to introduce mistuning, is shown for two levels of standard deviation (3% and 10%) with respect to the nominal value.

formulation described in Section 2.6. This strategy allows blade-to-blade variability to be incorporated directly at the component level.

The values of the frequency perturbation are obtained by performing numerical modal analyses of both the nominal and perturbed blade components using the full FE model. For each blade and for each retained free-interface mode, the perturbation parameter is defined as

$$\xi = \frac{\omega_{\text{pert}}^2 - \omega_{\text{nom}}^2}{\omega_{\text{nom}}^2}, \tag{46}$$

where ω_{nom} and ω_{pert} denote the natural frequencies of the nominal and perturbed blades, respectively. These perturbation factors are then used to modify the diagonal partition associated with the free-interface natural frequencies in the reduced stiffness matrix (Eq. 44), while all other reduced partitions are kept identical to those of the tuned model.

To assess the validity of the adopted mistuning assumption, namely that mistuning primarily affects the natural frequencies while not affecting the mode shapes, a comparison is performed between the nominal blade and two representative perturbed blades characterized by the extreme values of Young's modulus (blade 7 and blade 16, see Fig. 6). The comparison is carried out in terms of the MAC number for the first 20 elastic modes, as shown in Fig. 7. As can be observed, the MAC matrices exhibit a strong diagonal dominance, with values close to unity for the corresponding modes, indicating a high degree of correlation between the nominal and perturbed mode shapes. This result supports the underlying assumption that mistuning can be effectively modeled through perturbations of the free-interface natural frequencies while neglecting changes in the mode shapes.

Before presenting the results for the fully assembled mistuned bladed disk, the accuracy of this mistuning realization is first assessed at the component level. In particular, the natural frequencies and mode shapes of a perturbed blade predicted by the FE model are compared with those obtained from the reduced blade model, in which mistuning is introduced solely through the perturbed free-interface modal frequencies. This preliminary comparison provides a direct verification of the proposed mistuning implementation within the reduced-order framework.

The component-level results on individual blades reported in Fig. 8 demonstrate the capability of FIBM ROM to accurately represent the dynamics of a perturbed blade. For both small (σ = 3%) and large (σ = 10%) mistuning levels, the discrepancies between the natural frequencies predicted by the mistuned ROM and the full FEM remain extremely small, with relative errors of negligible magnitude across all considered modes and blades. In addition, the MAC values are consistently close to unity, indicating an excellent correlation between the mode shapes. Only minor localized deviations are observed, which remain limited and do not compromise the overall modal correspondence. Since a complete representation would require reporting 18 MAC matrices, which is not practical, only the diagonal terms are presented, as they directly quantify the correlation between corresponding modes.

The accuracy of the proposed mistuned ROM is further assessed at the assembly level by comparing its natural frequencies with those obtained from the full FEM of the mistuned bladed disk. The comparison is performed for both small (σ = 3%) and large (σ = 10%) mistuning levels, and the relative error is evaluated in terms of percentage difference in the natural frequencies with respect to the full FE reference solution. As shown in Fig. 9, the mistuned ROM is able to reproduce the eigenfrequencies of the full FE model of mistuned bladed disk with good accuracy for both mistuning scenarios. In the case of small mistuning, the mode-wise error remains well below 1% for all considered modes, with a mean error level close to 0.1%, indicating an excellent agreement between the reduced and full-order models. For the large mistuning case, slightly higher discrepancies are observed, as expected due to the stronger blade-to-blade variability; however, the maximum errors remain below 1%, and the mean error level stays below 0.3%.

The accuracy of the proposed mistuned ROM is then assessed in terms of mode shapes by evaluating the MAC between the ROM and the full FEM of the bladed disk. To this end, a single representative physical DOF per sector is selected to describe and track the displacement field associated with each mode. In particular, the chosen DOF is located at the blade tip, at the leading edge of the blade component, which is a common measurement location in experimental modal analysis [8].

The results for both small (σ = 3%) and large (σ = 10%) mistuning cases are shown in Fig. 10. For both configurations, the MAC values remain very close to unity for the vast majority of the considered modes, indicating an excellent correlation between the mode shapes predicted by the reduced and full-order models. Only a limited number of localized drops in the MAC value are observed, which are mainly associated with strongly localized modes, where small discrepancies in the spatial distribution of vibration may occur. Overall, these results demonstrate that the proposed ROM strategy is capable of accurately capturing the mode localization phenomenon induced by mistuning. In particular, the mistuned ROM is able to correctly identify the blades exhibiting the largest vibration amplitudes, which is a key requirement for reliable forced-response analysis and for the prediction of critical blades in mistuned bladed-disk assemblies.

The validity of the proposed ROM is finally assessed by comparing the forced response of the mistuned bladed disk under EO-type excitation. Engine orders ranging from EO-1 up to EO-$N/2$ (with N = 18) are considered, and both the ROM and the full FEM are excited using the same loading patterns. The steady-state response is computed by modal superposition, retaining the first 100 modes for both models. The modal damping ratio equal to 0.005 was used for each mode.

A fixed frequency bandwidth is selected, corresponding to the frequency range of the first modal family of the tuned assembly. Although other modal families can also be investigated, the results presented here focus on the first family to clearly assess the capability of the ROM within a representative frequency range. The comparison between the ROM and full FEM forced responses for both small and large mistuning cases is shown in Fig. 11. An excellent agreement is observed across all EOs, both in terms of resonance frequencies and response amplitudes. In particular, the characteristic mode splitting [34] induced by mistuning is accurately reproduced by the ROM, with multiple closely spaced resonance peaks clearly captured for all EOs.

Moreover, the excitation of multiple modes within the considered bandwidth can be explained by the loss of the monoharmonic nature of the mode shapes in mistuned systems. In a tuned bladed disk, each mode shape is characterized by a single nodal diameter (ND) harmonic, resulting in a purely monoharmonic spatial distribution. Consequently, the EO

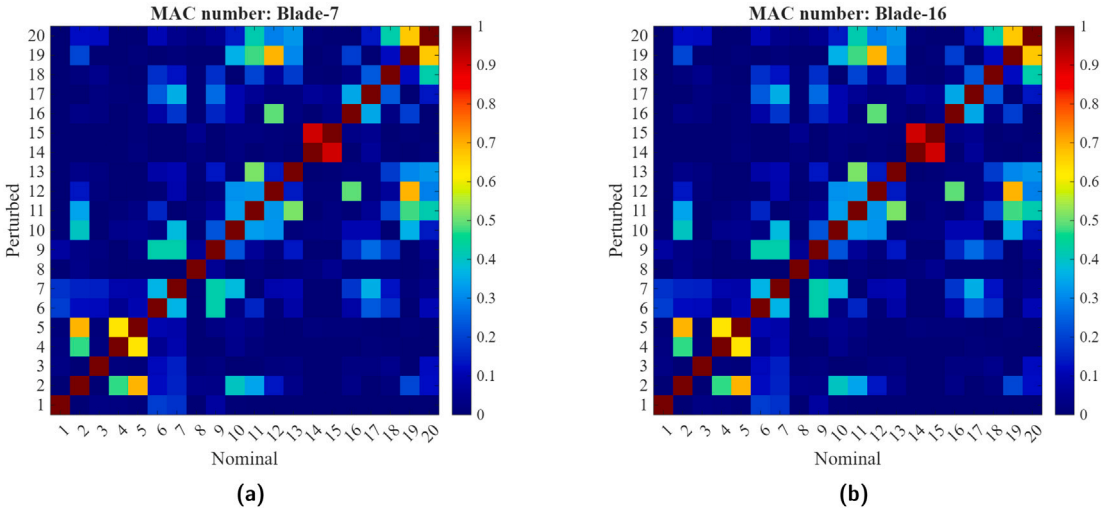


Fig. 7. Modal Assurance Criterion (MAC) between nominal and perturbed blade mode shapes: (a) blade 7 (maximum Young's modulus deviation) and (b) blade 16 (minimum Young's modulus deviation).

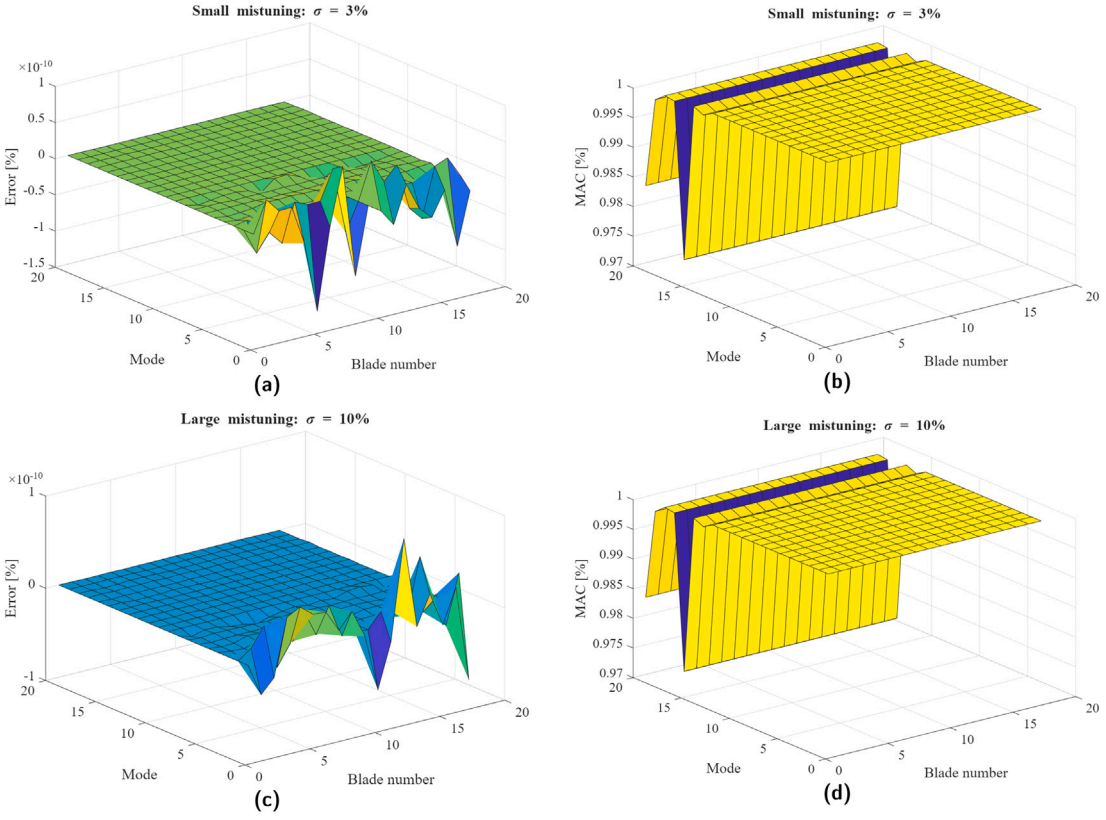


Fig. 8. Validation of perturbed blade components in the ROM: mode-wise percentage error between ROM and full FEM blade natural frequencies for (a) small mistuning (σ = 3%) and (c) large mistuning (σ = 10%); corresponding MAC values between ROM and full FEM blade mode shapes for (b) small mistuning and (d) large mistuning.

excitation, which is also characterized by a specific pattern, resembling the ND mode, is orthogonal to all other ND modes, and only the corresponding mode is excited. In contrast, in a mistuned system, the mode shapes are no longer purely monoharmonic but can be represented as a superposition of multiple ND harmonics. As a result, each mistuned mode contains contributions from several ND components, including those associated with other modes. This leads to a non-zero projection of the EO excitation onto multiple modes, thereby causing the simultaneous excitation of several modes within the same frequency range. This effect becomes more pronounced in the case of large mistuning, where stronger modal coupling and localization phenomena occur. Despite this increased complexity, the ROM is still able to closely match the full FE response, demonstrating its robustness and accuracy in predicting forced response characteristics of mistuned bladed disks.

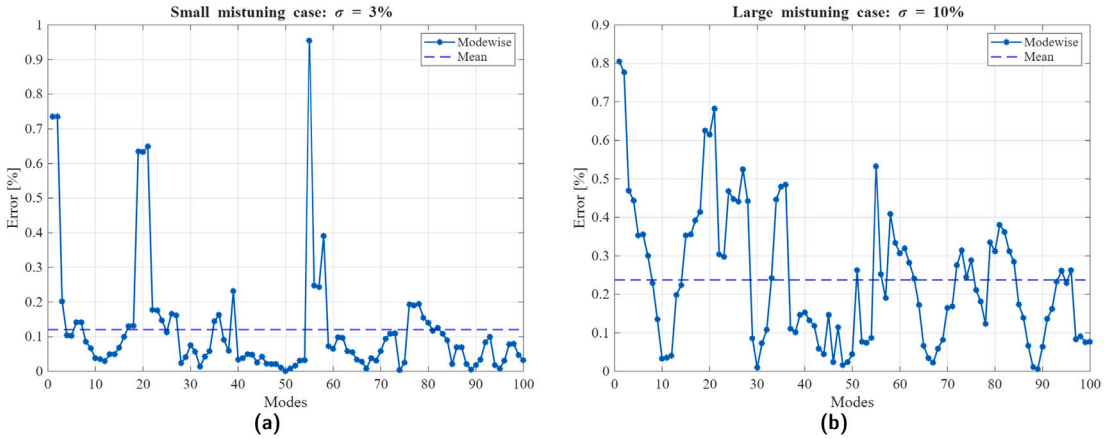


Fig. 9. Mode-wise percentage absolute error between the natural frequencies predicted by the mistuned ROM and the full FE model of the bladed disk for (a) small mistuning ($\sigma = 3\%$) and (b) large mistuning ($\sigma = 10\%$).

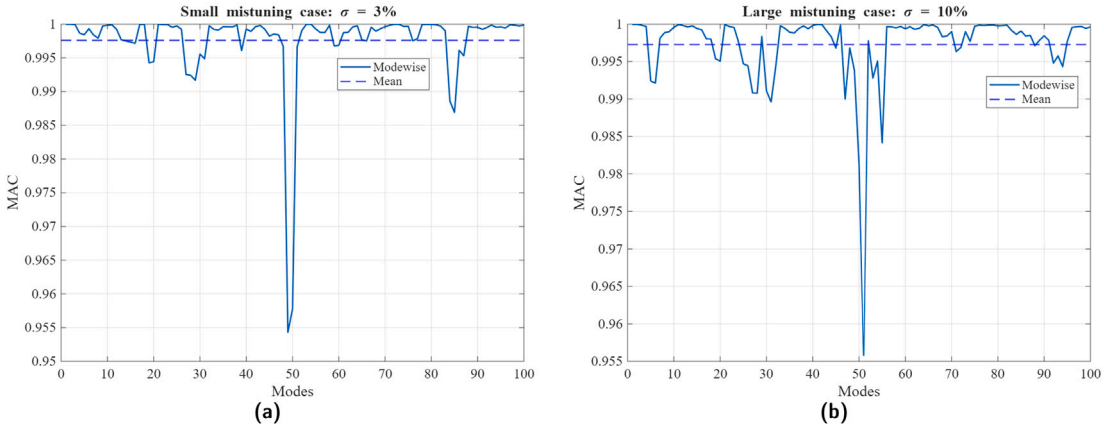


Fig. 10. Mode-wise MAC values between the mistuned ROM and the full FE model of the bladed disk, computed using one representative degree of freedom per sector for (a) small mistuning ($\sigma = 3\%$) and (b) large mistuning ($\sigma = 10\%$).

Overall, the results presented in this section demonstrate the effectiveness and robustness of the proposed ROM strategy for the analysis of mistuned bladed disks. The ROM is shown to accurately reproduce the dynamic characteristics of the full FEM at both the component and assembly levels, including natural frequencies, mode shapes, and forced response functions.

4. Conclusion

This work has presented a comprehensive ROM framework for the dynamic analysis of mistuned bladed disks, addressing both accuracy and computational efficiency limitations commonly encountered in full FE simulations. The proposed approach, referred to as the Free-Interface Blade Mistuning (FIBM) method, is built upon a component-level reduction strategy that combines the Rubin free-interface reduction for the blade with the Craig–Bampton reduction for the disk sector, complemented by a Gram–Schmidt Interface reduction of the cyclic symmetry frontiers.

An important contribution of this work lies in the systematic and explicit analytical formulation of the reduced and assembled mass and stiffness matrices, where all matrix partitions in the present framework are fully expanded and expressed in closed form. This explicit representation provides a clear insight into the role of each substructure and interface contribution, enables tracking of intermediate assembly steps, and facilitates efficient implementation when computational resources are limited or when repeated evaluations of the reduced model are required.

The use of free-interface blade modes constitutes another important advancement of the proposed methodology. By relying on free–free blade modal properties, the reduction basis is independent of artificial boundary constraints and retains a direct physical interpretation. This feature is particularly advantageous from an experimental perspective, as free-interface blade modes can be identified without uncertainties related to fixture conditions. Moreover, the diagonal structure of the reduced blade stiffness matrix associated with the free-interface natural frequencies enables a straightforward and physically consistent introduction of mistuning effects.

Within this framework, blade mistuning is incorporated through perturbations of the free-interface blade natural frequencies, evaluated from comparisons between tuned and mistuned blade FEMs. This strategy allows blade-to-blade variability to be introduced locally at the component level, without modifying the reduction basis or affecting the disk reduction. As a result, the proposed approach maintains a modular structure and is well suited for parametric and probabilistic analyses involving multiple mistuning realizations.

The accuracy of the FIBM method has been thoroughly validated against a high-fidelity full FEM of a mistuned bladed disk. Validation has been performed at both the component and assembly levels, considering tuned and mistuned configurations. The ROM accurately reproduces the natural frequencies and mode shapes of the full model, with very low

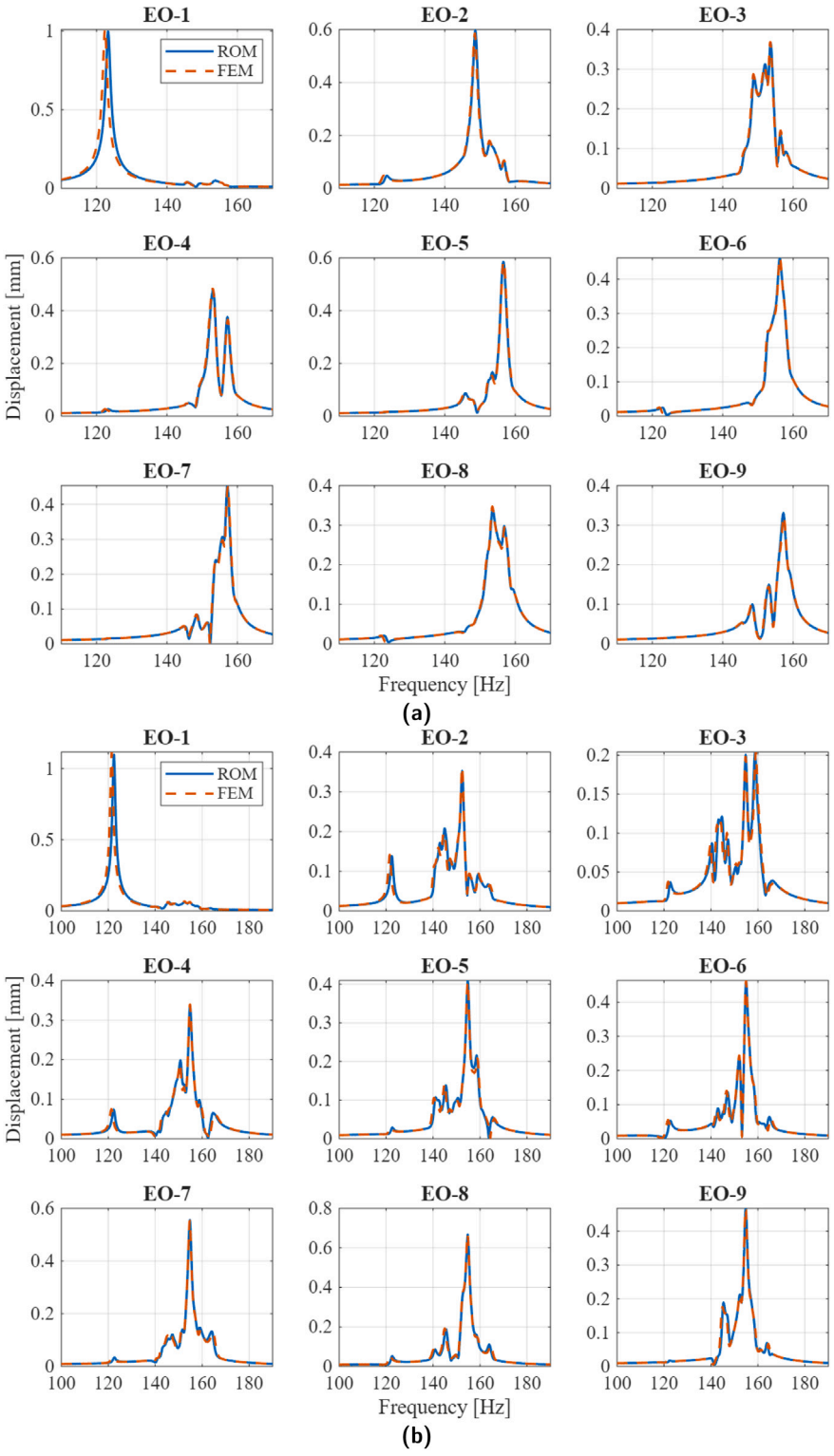


Fig. 11. Comparison of engine-order forced response functions obtained from the ROM and the full FE model for the first modal family of the mistuned bladed disk: (a) small mistuning ($\sigma = 3\%$) and (b) large mistuning ($\sigma = 10\%$).

relative errors and consistently high MAC values, even in the presence of large mistuning levels. These results confirm that the essential dynamic characteristics of the system are preserved despite the significant reduction in model size.

At the assembly level, the proposed ROM successfully captures key mistuning-induced phenomena, including mode splitting, modal coupling, and vibration localization. The forced response analysis under EO excitation further demonstrates the robustness of the approach. The reduced model accurately predicts resonance frequencies, response amplitudes, and the excitation of multiple modes within a given frequency band. These effects become more pronounced for large mistuning levels, yet remain well captured by the proposed reduced-order formulation.

From a computational standpoint, the developed framework achieves a drastic reduction in system size while maintaining high predictive

accuracy. This reduction enables efficient computation of free and forced responses and makes large-scale parametric studies, uncertainty quantification, and mistuning sensitivity analyses feasible, which would otherwise be prohibitive with full FE models.

In summary, the proposed Free-Interface Blade Mistuning approach provides a robust, accurate, and computationally efficient tool for the dynamic analysis of mistuned bladed-disk assemblies. By combining free-interface reduction, explicit analytical assembly, and a physically consistent mistuning representation, the method bridges the gap between high-fidelity FE modeling and practical reduced-order analysis. The proposed FIBM formulation can also be employed for nonlinear forced response analyses of mistuned bladed disks. The effects of blade–disk friction can be represented through an equivalent modal damping imposed on the linear system, which is a common practice in many industrial applications, while a more detailed representation can be achieved by introducing nonlinear contact elements at the blade–disk interfaces without modifying the proposed reduced-order representation and mistuning formulation. Standard nonlinear solution procedures, such as the Harmonic Balance Method or direct time integration, can then be adopted to compute the dynamic response.

CRediT authorship contribution statement

Umidjon Usmanov: Writing – original draft, Validation, Software, Methodology, Investigation, Formal analysis, Data curation, Conceptualization. **Giuseppe Battiato:** Writing – review & editing, Validation, Supervision, Resources, Investigation, Conceptualization. **Christian Maria Firrone:** Writing – review & editing, Validation, Supervision, Resources, Methodology, Investigation, Conceptualization.

Declaration of competing interest

The authors declare that they have no known competing financial interests or personal relationships that could have appeared to influence the work reported in this paper.

Data availability

Data will be made available on request.

References

[1] Allen MS, Rixen DJ, van der Seijs M, Tiso P, Abrahamsson T, Mayes RL. Substructuring in engineering dynamics: emerging numerical and experimental techniques, CISM International Centre for Mechanical Sciences. vol. 2020. Cham: Springer; 2020.

[2] Battiao G, Firrone CM, Berruti TM, Epureanu BI. A general method for sub-systems coupling for the dynamic analysis. In: Proceedings of ISMA 2016. Leuven, Belgium; 2016.

[3] Battiato G, Firrone C. Reduced order modeling of large contact interfaces to calculate the non-linear response of frictionally damped structures. Procedia Struct Integr 2019;24:837–51. https://www.sciencedirect.com/science/article/pii/S2452321620302997.

[4] Battiato G, Firrone C. A modal based reduction technique for wide loose interfaces and application to a turbine stator. Mech Syst Signal Process 2020;139:106415. https://www.sciencedirect.com/science/article/pii/S0888327019306363.

[5] Battiato G, Firrone CM. Reduced order modeling for forced response prediction of structures with large contact interfaces. In: Proceedings of ISMA2018 - 28th international conference on noise and vibration engineering. Leuven, Belgium; 2018.

[6] Bladh R, Castanier MP, Pierre C. Reduced order modeling and vibration analysis of mistuned bladed disk assemblies with shrouds. J Eng Gas Turbines Power 1999;121:515–22. https://doi.org/10.1115/1.2818503

[7] Bladh R, Castanier MP, Pierre C. Component-mode-based reduced order modeling techniques for mistuned bladed disks: Part I — Theoretical models. In: Proceedings of the ASME turbo expo 2000; 2000. https://doi.org/10.1115/2000-GT-0360, p. V004T03A006.

[8] Bladh R, Castanier MP, Pierre C. Component-mode-based reduced order modeling techniques for mistuned bladed disks: Part II — Application. In: Proceedings of the ASME turbo expo 2000; 2000. https://doi.org/10.1115/2000-GT-0361, p. V004T03A007.

[9] Castanier MP, Óttarsson G, Pierre C. A reduced order modeling technique for mistuned bladed disks. J Vib Acoust 1997;119:439–47. https://doi.org/10.1115/1.2889743

[10] Craig RR, Bampton MCC. Coupling of substructures for dynamic analyses. AIAA J 1968;6:1313–9. https://doi.org/10.2514/3.4741

[11] Craig RR, Kurdila AJ ed. Fundamentals of structural dynamics. 2 ed. Hoboken, NJ: John Wiley & Sons; 2006.

[12] Dye RCF, Henry TA. Vibration amplitudes of compressor blades resulting from scatter in blade natural frequencies. J Eng Power 1969;91:182–7. https://doi.org/10.1115/1.3574726

[13] El-Bayoumy LE, Srinivasan AV. Influence of mistuning on rotor-blade vibrations. AIAA J 1975;13:460–4. https://doi.org/10.2514/3.49731

[14] Ewins D. The effects of detuning upon the forced vibrations of bladed disks. J Sound Vib 1969;9:65–79. https://doi.org/10.1016/0022-460X(69)90264-8

[15] Ewins DJ. Vibration characteristics of bladed disc assemblies. J Mech Eng Sci 1973;15:165–86. https://doi.org/10.1243/JMES_JOUR_1973_015_032_02

[16] Ewins DJ, Han ZS. Resonant vibration levels of a mistuned bladed disk. J Vib Acoust Stress Reliab Des 1984;106:211–7. https://doi.org/10.1115/1.3269171

[17] Feiner DM, Griffin JH. A fundamental model of mistuning for a single family of modes. J Turbomach 2002;124:597–605. https://doi.org/10.1115/1.1508384

[18] Griffin JH, Hoosac TM. Model development and statistical investigation of turbine blade mistuning. J Vib Acoust Stress Reliab Des 1984;106:204–10. https://doi.org/10.1115/1.3269170

[19] Kenyon JA, Griffin JH. Forced response of turbine engine bladed disks and sensitivity to harmonic mistuning. J Eng Gas Turbines Power 2002;125:113–20. https://doi.org/10.1115/1.1498269

[20] Krizak T, D'souza K. A generalized model of mistuning for bladed disks. J Sound Vib 2025;606:119003. https://www.sciencedirect.com/science/article/pii/S0022460X2500077X.

[21] Kruse M, Pierre C. Forced response of mistuned bladed disks using reduced-order modeling. American Institute of Aeronautics and Astronautics; 1996. https://arc.aiaa.org/doi/abs/10.2514/6.1996-1545.

[22] Lim S, Bladh R, Castanier M, Pierre C. A compact, generalized component mode mistuning representation for modeling bladed disk vibration. AIAA 2003;2:1359–80.

[23] Long W, Chen Y. Reduced order modeling and mistuning identification method for rotating bladed disks under varying speeds. J Sound Vib 2025;595:118687. https://www.sciencedirect.com/science/article/pii/S0022460X24004498.

[24] MacBain JC, Whaley PW. Maximum resonant response of mistuned bladed disks. J Vib Acoust Stress Reliab Des 1984;106:218–23. https://doi.org/10.1115/1.3269172

[25] Mashayekhi F, Nobari A, Zucca S. Hybrid reduction of mistuned bladed disks for nonlinear forced response analysis with dry friction. Int J Non-Linear Mech 2019;116:73–84. https://www.sciencedirect.com/science/article/pii/S0020746219301179.

[26] Petrov EP, Ewins DJ. Analysis of the worst mistuning patterns in bladed disk assemblies. J Turbomach 2003;125:623–31. https://doi.org/10.1115/1.1622710

[27] Petrov EP, Sanliturk KY, Ewins DJ. A new method for dynamic analysis of mistuned bladed disks based on the exact relationship between tuned and mistuned systems. J Eng Gas Turbines Power 2002;124:586–97. https://doi.org/10.1115/1.1451753

[28] Pinto V, Battiato G, Firrone CM. A reduction technique for the calculation of the forced response of bladed disks in the presence of contact mistuning at blade root joints. J Eng Gas Turbines Power 2022;145:021013. https://doi.org/10.1115/1.4055722

[29] Pinto V, Battiato G, Firrone CM. Reduced order models for bladed disks with contact mistuning at blade root joints. In: Proceedings of the ASME turbo expo 2023; 2023. https://doi.org/10.1115/GT2023-103078, p. V11BT23A006.

[30] Pourkiaee SM, Zucca S, Parker RG. Relative cyclic component mode synthesis: a reduced order modeling approach for mistuned bladed disks with friction interfaces. Mech Syst Signal Process 2022;163:108197. https://www.sciencedirect.com/science/article/pii/S0888327021005732.

[31] Rubin S. Improved component-mode representation for structural dynamic analysis. AIAA J 1975;13:995–1006. https://doi.org/10.2514/3.60497

[32] Saletti G, Pourkiaee M, Zucca S. Mass mistuning reduced order models for bladed disks with shroud friction joints. In: Proceedings of the ASME turbo expo 2024; 2024. https://doi.org/10.1115/GT2024-123976, p. V10BT27A011.

[33] Tobias SA, Arnold RN. The influence of dynamical imperfection on the vibration of rotating disks. Proc Inst Mech Eng 1957;171:669–90. https://doi.org/10.1243/PIME_PROC_1957_171_056_02

[34] Vargiu P, Firrone C, Zucca S, Gola M. A reduced order model based on sector mistuning for the dynamic analysis of mistuned bladed disks. Int J Mech Sci 2011;53:639–46. https://www.sciencedirect.com/science/article/pii/S0020740311000993.

[35] Voormeer SN. Dynamic substructuring methodologies for integrated dynamic analysis of wind turbines [Ph.D. thesis]. Delft, The Netherlands: Delft University of Technology; 2012.

[36] Wagner JT. Coupling of turbomachine blade vibrations through the rotor. J Eng Power 1967;89:502–12. https://doi.org/10.1115/1.3616718

[37] Whitehead DS. Effect of mistuning on the vibration of turbo-machine blades induced by wakes. J Mech Eng Sci 1966;8:15–21. https://doi.org/10.1243/JMES_JOUR_1966_008_004_02

[38] Yang MT, Griffin JH. A reduced order approach for the vibration of mistuned bladed disk assemblies. J Eng Gas Turbines Power 1997;119:161–7. https://doi.org/10.1115/1.2815542

[39] Yang MT, Griffin JH. A reduced-order model of mistuning using a subset of nominal system modes. J Eng Gas Turbines Power 1999;123:893–900. https://doi.org/10.1115/1.1385197